

Beyond radial profiles: Using log-normal distributions to model the multiphase circumgalactic medium

Alankar Dutta¹★, Mukesh Singh Bisht²†, Prateek Sharma¹‡, Ritoli Ghosh¹,
Manami Roy², and Biman B. Nath²

¹Department of Physics, Indian Institute of Science, Bangalore, KA 560012, India

²Raman Research Institute, Bangalore, KA 560080, India

Accepted XXX. Received YYY; in original form ZZZ

ABSTRACT

Recent observations and simulations reveal that the circumgalactic medium (CGM) surrounding galaxies is multiphase, with the gas temperatures spanning a wide range at most radii, $\sim 10^4$ K to the virial temperature ($\sim 10^6$ K for Milky Way). Traditional CGM models using simple density profiles are inadequate at reproducing observations that indicate a broad temperature range. Alternatively, a model based on probability distribution functions (PDFs) with parameters motivated by simulations can better match multi-wavelength observations. In this work, we use log-normal distributions, commonly seen in the simulations of the multiphase interstellar and circumgalactic media, to model the multiphase CGM. We generalize the isothermal background model by Faerman et al. 2017 to include more general CGM profiles. We extend the existing probabilistic models from 1D-PDFs in temperature to 2D-PDFs in density-temperature phase space and constrain its parameters using a Milky Way-like Illustris TNG50–1 halo. We generate various synthetic observables such as column densities of different ions, UV/X-ray spectra, and dispersion and emission measures. X-ray and radio (Fast Radio Burst) observations mainly constrain the hot gas properties. However, interpreting cold/warm phase diagnostics is not straightforward since these phases are patchy, with inherent variability in intercepting these clouds along arbitrary lines of sight. We provide a tabulated comparison of model predictions with observations and plan to expand this into a comprehensive compilation of models and data. Our modeling provides a simple analytic framework that is useful for describing important aspects of the multiphase CGM.

Key words: Galaxy: halo – galaxies: haloes – quasars: absorption lines – methods: data analysis – methods: analytical – software: development

1 INTRODUCTION

Several independent observational probes over the last decade have uncovered the circumgalactic medium (CGM hereafter), the diffuse atmospheres around galaxies like our Milky Way (for a review, see Tumlinson et al. 2017 and Faucher-Giguère & Oh 2023). Being diffuse, the CGM is hard to detect but is the major baryonic component of the galactic halos, making up to a few times more mass than the combined mass of the stars and the interstellar medium (ISM; Werk et al. 2014; Das et al. 2020).

Traditionally, the CGM is modeled with a parametric density

profile/distribution of the volume-filling hot phase (Maller & Bullock 2004; Henley & Shelton 2010; Sharma et al. 2012b; Gupta et al. 2012; Miller & Bregman 2013; Mathews & Prochaska 2017; Yao et al. 2017; Stern et al. 2019; Yamasaki & Totani 2020; Faerman et al. 2020). This approach is incomplete because observations (e.g., Werk et al. 2014; Tumlinson et al. 2013) show that most of the sightlines intercept not only the hot phase but also the ions tracing the cold/warm phase ($10^4 - 10^{5.5}$ K). Traditional models that only include the hot phase, therefore, fail to explain the ubiquity of the cooler phases in observations. Presently, there are only piecemeal physical models to account for the cold/warm phases. For instance, to explain the observed OVI (O^{+5}) column densities, Faerman et al. 2017 propose an ad hoc introduction of a $10^{5.5}$ K phase. Likewise, Faerman & Werk 2023 presume a fixed volume fraction for the cold phase in ionization/thermal equilibrium. Since the cold phase has

★ E-mail: alankardutta@iisc.ac.in (AD)

† E-mail: msbisht@rrimail.rii.res.in (MB)

‡ E-mail: prateek@iisc.ac.in (PS)

low thermal pressure, it is necessary to have a large non-thermal support to maintain the total pressure balance with the hot phase. However, the conclusions drawn from such models depend heavily on the model assumptions. Therefore, generating multi-wavelength observables from a diverse range of physical models is imperative.

To address the limitation of simple profiles to describe a multi-phase CGM, we generalize the model of [Faerman et al. \(2017\)](#) based on a log-normal volume distribution across the complete range of CGM temperatures. This model is physically well-motivated, since log-normal distribution of densities and temperatures are routinely inferred from observations and simulations of different phases of the ISM ([Körtgen et al. 2017](#); [Chen et al. 2018](#)) and the CGM ([Das et al. 2021b](#); [Vijayan & Li 2022](#); [Mohapatra et al. 2022](#)). Further, a log-normal temperature distribution captures the “core” (up to a quadratic order Taylor series expansion in $\ln T$) of a generic peaked temperature distribution. Because of the central limit theorem, log-normal distributions are understood as a natural outcome of generic multiplicative random walk processes. Additionally, log-normal distributions are a useful choice for modeling the multiphase CGM, as the weighted integrals of log-normal PDFs (probability distribution functions) involved in calculating different synthetic observables are analytically tractable.

Since each observational probe gives a somewhat biased view of the CGM, there is a need for a library of CGM models that can be tested against diverse multi-wavelength observations, ranging from radio ([Bhardwaj et al. 2021](#); [Wu & McQuinn 2022](#)), mm ([Singh et al. 2018](#); [Amodeo et al. 2021](#)), UV ([Wakker et al. 2003](#); [Wakker & Savage 2009](#); [Werk et al. 2014](#); [Muzahid et al. 2018](#); [Burchett et al. 2019](#); [Chen et al. 2020](#); [Lehner et al. 2020](#); [Cooper et al. 2021](#); [Haislmaier et al. 2021](#); [Sameer et al. 2021](#)), optical ([Kacprzak et al. 2015a](#); [Lehner et al. 2015](#); [Nielsen et al. 2017](#); [Zabl et al. 2019](#); [Péroux et al. 2019](#); [Nateghi et al. 2020](#)) to X-rays ([Gupta et al. 2012](#); [Kaaret et al. 2020](#); [Ponti et al. 2023b](#)). Observations (e.g., [Werk et al. 2014](#); [Kacprzak et al. 2015b](#); [Das et al. 2021b](#); [Bluem et al. 2022](#); [Qu et al. 2024](#)) and numerical simulations (e.g., [Schaye et al. 2015](#); [Oppenheimer et al. 2018](#); [van de Voort et al. 2018](#); [Stern et al. 2019](#); [Hummels et al. 2019](#); [Nelson et al. 2020](#); [Lochhaas et al. 2020](#); [Marra et al. 2021](#); [DeFelippis et al. 2021](#); [Augustin et al. 2021](#); [Saeedzadeh et al. 2023](#)) reveal that the CGM has a complex kinematic and multiphase structure, with multiple temperature components with different line of sight velocities present along most sightlines. This highlights the need for models that go beyond simple radial density/temperature profiles. In this work, we demonstrate that a probabilistic description utilizing distribution functions can better describe the multiphase CGM (the existing work in this direction is rather limited; e.g., [Faerman et al. 2017](#); [Vijayan & Li 2022](#)).

We generalize the [Faerman et al. \(2017\)](#) (FSM17 hereafter) model of the CGM to allow for different phases in any generic thermodynamic state. In the FSM17 model, the baseline isothermal log-normal PDF of the hot phase is modified to include an additional warm log-normal component at $10^{5.5}$ K. To demonstrate the flexibility of our generalization, we replace the isothermal baseline model of FSM17 with an isentropic profile (following [Faerman et al. 2020](#)) but retain the same prescription for the modified warm component. Our generalization can incorporate any arbitrary thermodynamic relation between phases. Specifically, we consider the hot and warm phases to be either isochoric or isobaric with respect to each other. We then compare the observables from all these models (OVI/VII/VIII/NV column densities, X-ray emission measure [EM], emission spectra, and dispersion measure [DM]) with the observed data.

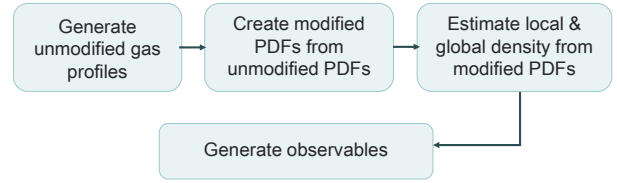


Figure 1. Flowchart of the procedure proposed in [FSM17](#) to produce a warm phase from an isothermal unmodified profile (see section 2.1). We generalize the [FSM17](#) procedure to model any generic thermodynamic profile of the CGM (see section 2.2) with the flexibility to have an arbitrary pressure-density relation across the phases (see section 2.3). Synthetic observables can be generated to match against observations after profiles are computed (see section 2.4).

We next construct a one-zone, three-phase model comprising hot ($\sim 10^6$ K), warm ($\sim 10^5$ K), and cold ($\sim 10^4$ K) gas. Each phase is modeled as a two-dimensional log-normal PDF in the density-temperature ($\rho - T$) phase space. We adjust the volume fraction and the median density and temperature along with their corresponding spreads for each phase to match the $\rho - T$ distribution measured for a Milky Way-like halo from the *Illustris* TNG50-1 cosmological simulation ([Nelson et al. 2020](#)). From this fitted three-phase model, we generate column densities of OVI and MgII (the warm and cold gas tracers, respectively), estimate the EM, DM, and X-ray surface brightness, and compare with the observations. Additionally, we formulate a simple, approximate prescription to move beyond the one-zone approximation in our three-phase model of the CGM.

Our paper is organized as follows. Section 2 explains the two-phase FSM17 model and introduces our generalized framework and the integrals needed to generate observables from the PDFs. Section 3 introduces the three-phase model with 2D (in density-temperature space) log-normal distribution for each phase, calibrated with a simulated Milky Way-like halo from *Illustris* TNG50-1 cosmological simulation. Section 4 discusses the implications of our work for the multiphase CGM, in particular, the influence of warm/cold clouds with a small volume filling fraction. Section 5 concludes with a summary of our work.

2 GENERALIZED FAERMAN MODELS

In this section, we elaborate on the model introduced by [FSM17](#). We list the symbols and notation used to reformulate the [FSM17](#) model in Tab. 1, crucial for generalizing to a broad class of probabilistic CGM models. Fig. 1 outlines the steps discussed in section 2.1 for generating these probabilistic models. As a specific example, in section 2.2 we replace the isothermal hot gas profile in [FSM17](#) with an isentropic profile but retain the same prescription for the warm gas. In section 2.3, we emphasize the implication of choosing isochoric or isobaric radiative cooling to generate the warm phase. The thermodynamic state of the hot and the warm gas used in these models can significantly alter synthetic observables, as discussed in section 2.4.

2.1 FSM17 model for the CGM

Here we list the different steps involved in using the [FSM17](#) model to study the CGM (see Fig. 1):

- (i) *Create unmodified hydrostatic profiles* for the volume-filling gas in the CGM. We denote unmodified profiles with superscript (u),

Table 1. Symbols & notation used for probabilistic models

Symbol(s)	Meaning
r	distance from the halo center
$\rho^{(u)}, p^{(u)}, T^{(u)}$	unmodified profiles of hot CGM
$\mathcal{P}_V^{(u)}(T), \mathcal{P}_M^{(u)}(T)$	temperature-PDF (T-PDF) of unmodified gas weighed by volume (V) or mass (M)
$\mathcal{P}_V^{(w)}(T), \mathcal{P}_V^{(h)}(T)$	modified T-PDF weighed by V of the warm or hot phases
$\langle \rangle, \langle \rangle_M$	average weighed by V or M
$T_{\text{med},V}^{(u)}, T_{\text{med},V}^{(w)}$	median temperature T of unmodified or warm gas T-PDF weighed by V
$\mathcal{N}(x, \sigma)$	Gaussian PDF, mean 0 and standard deviation σ
$\mathcal{N}(x, \mu, \sigma)$	Gaussian PDF, mean μ and standard deviation σ
σ_u, σ_w	standard deviations of the unmodified or warm gas T-PDFs
T_c	cutoff temperature below which unmodified PDF is modified ($t_{\text{cool}}(T_c)/t_{\text{ff}} = \text{cutoff}$)
$dM^{(i)}, dV^{(i)}$	mass, volume for a phase in temperature range $[T, T + dT]$
$dM = \sum dM^{(i)}$	total mass in range $[T, T + dT]$
$dV = \sum dV^{(i)}$	total volume in range $[T, T + dT]$
$M^{(i)}, V^{(i)}$	total mass, volume for a phase across all T s
$M = \sum M^{(i)}$	total mass including all phases across all T s
$V = \sum V^{(i)}$	total volume including all phases across all T s
$f_M^{(i)} = M^{(i)}/M$	mass fraction in a phase
$f_V^{(i)} = V^{(i)}/V$	volume fraction in a phase
$\langle \rho^{(i)} \rangle = M^{(i)}/V^{(i)}$	local average density of a particular phase
$\langle \rho^{(i)} \rangle_g = M^{(i)}/V$	global average density of a particular phase

such as $p^{(u)}, \rho^{(u)}, T^{(u)}$. Such unmodified profiles can be prescribed by any generic CGM model, like the precipitation model (Sharma et al. 2012b; Voit 2019) or the isentropic model (Faerman et al. 2020). FSM17 used isothermal gas in hydrostatic equilibrium as the unmodified profile. The total pressure p_{tot} considered by FSM17 has thermal, non-thermal (e.g., due to magnetic fields and cosmic rays), and turbulent components such that $p_{\text{tot}} = p_{\text{th}} + p_{\text{nth}} + p_{\text{turb}}$, where $p_{\text{nth}} = (\alpha - 1)p_{\text{th}}$, $p_{\text{turb}}/p_{\text{th}} = (\sigma_{\text{turb}}/\sigma_{\text{th}})^2$, and $p_{\text{th}} = p_{\text{tot}}/(\alpha + \sigma_{\text{turb}}^2/\sigma_{\text{th}}^2)$. In this isothermal model, the total pressure is given by the simple hydrostatic solution,

$$p_{\text{tot}}^{(u)}(r) = p_{0,\text{tot}}^{(u)} \exp\left(-\frac{[\Phi(r) - \Phi_0]}{c_t^2}\right), \quad (1)$$

where c_t is the effective isothermal sound speed, taking into account the contributions from the non-thermal and turbulent pressures, and the subscript 0 refers to a reference radius with the total pressure $p_{0,\text{tot}}^{(u)}$ and the potential Φ_0 . Therefore, the effective sound speed in Eq. (1) is $c_t^2 = \alpha\sigma_{\text{th}}^2 + \sigma_{\text{turb}}^2$ (here we use the same notation as FSM17). Tab. 2 lists our parameter values, which are taken from the fiducial models in FSM17 and FSM20, chosen mainly to match the column density of OVI. The non-thermal pressure support due to cosmic rays (e.g., Salem et al. 2015; Ji et al. 2020; Butsky et al. 2022) or turbulence (easier to detect in clusters, e.g., Li et al. 2020; ZuHone et al. 2018; Mohapatra et al. 2021 than in CGM, e.g., Buie et al. 2020a,b; Chen et al. 2023) in the CGM can be significant.

The thermal pressure and density are related by the ideal gas equation of state $p_{\text{th}}^{(u)} = \rho^{(u)} k_B T^{(u)} / \mu m_p$. The temperature $T^{(u)}$

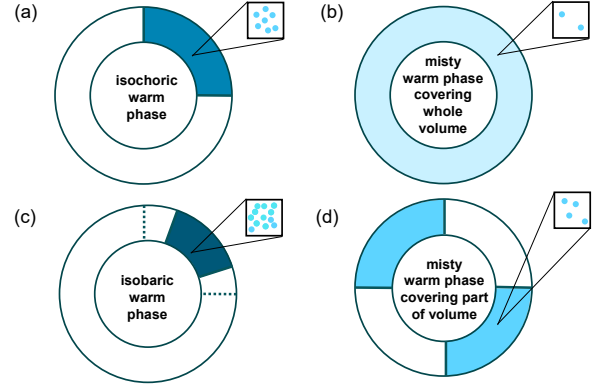


Figure 2. Cartoon illustrations of various kinds of modifications to introduce warm gas in any shell of our CGM model: the warm phase condenses out of the hot phase and is either (a) *isochoric* or (c) *isobaric* relative to the hot phase. Being isobaric with the hot phase, the warm phase has a higher density and occupies a smaller volume, as indicated by the darker shade of blue in (c). The warm gas may occupy only a part of the shell volume (as in (a), (c), and (d)) rather than being distributed uniformly (the *mist limit*; shown in (b)). The inset squares in the top right corner of each sub-figure indicate the densities of warm gas in different cases.

here is the mass-weighted average temperature at each radius, which also determines the thermal broadening $\sigma_{\text{th}}^2 = k_B T^{(u)} / \mu m_p$ of the unmodified gas. The temperature is assumed to be constant in the unmodified profile used in FSM17. We later also use an isentropic unmodified profile (see section 2.2) from Faerman et al. 2020 (FSM20 hereafter) to illustrate the procedure for a general unmodified profile.

(ii) *Unmodified log-normal temperature-PDFs*: After obtaining the unmodified profiles, FSM17 assumes a log-normal volume distribution of temperature in each radial shell of the CGM. The motivation behind this is that the non-thermal and turbulent processes in the CGM cause fluctuations around the unmodified gas properties and results in a locally peaked temperature/density distribution. Therefore, we describe the gas temperature distribution in each shell by a log-normal PDF and multiphase gas exists co-spatially at all radii. A perfectly uniform multiphase shell is an approximation, and the cooler phases are expected to be spatially inhomogeneous (e.g., see Figure 2). We quantify the amount of such co-spatial multiphase gas at any radius r by the volume/mass fraction of the gas in the temperature range $[T, T + dT]$. The gas distribution is assumed to be log-normal (in volume and consequently also in mass) at all radii from the center of the CGM and the volume PDF (see the light red line in Figure 3) can be expressed as

$$\mathcal{P}_V^{(u)}(T) = \frac{1}{T} \mathcal{N}(x, \sigma_u), \quad (2)$$

where $x \equiv \ln(T/T_{\text{med},V}^{(u)})$, $T_{\text{med},V}^{(u)}$ is the median temperature in the volume PDF (since $\mathcal{P}_V^{(u)}(T)dT = \mathcal{N}(x, \sigma_u)dx$; see Tab. 1 for the notation), and

$$\mathcal{N}(x, \sigma_u) = \frac{1}{\sqrt{2\pi}\sigma_u} \exp\left(-\frac{x^2}{2\sigma_u^2}\right) \quad (3)$$

is the normal distribution with zero mean and standard deviation σ_u . Note that the distribution in $\ln T$ space, $\mathcal{P}_V^{(u)}(\ln[T/T_{\text{med},V}^{(u)}]) = T\mathcal{P}_V^{(u)}(T) = \mathcal{N}^{(u)}(x, \sigma_u)$, is Gaussian. In the FSM17 prescription, the unmodified gas at every radius is assumed to be isobaric so that

Table 2. Parameters of the two-phase CGM models

Input Parameters	$\gamma = 1$	$\gamma = 5/3$
halo mass M_{200}	$10^{12} M_{\odot}$	$10^{12} M_{\odot}$
CGM radius r_{CGM}	$1.1 \times r_{200}^{\dagger}$	$1.1 \times r_{200}$
$p_{0,\text{tot}}^{(u)}$	4580 K cm^{-3}	-
r_0 (reference radius)	8.5 kpc	8.5 kpc
$\alpha \equiv 1 + p_{\text{nt}}/p_{\text{th}}$	1.9	2.1
$T(r_{\text{CGM}})$	-	$2.4 \times 10^5 \text{ K}$
$n_H(r_{\text{CGM}})$	-	$1.1 \times 10^{-5} \text{ cm}^{-3}$
σ_{turb}	60 km s^{-1}	60 km s^{-1}
$\ddagger Z(r_{\text{CGM}})$	0.3	0.3
$Z_0 \equiv Z(r_0)$	1	1
redshift	0.2	0.2
cutoff ($t_{\text{cool}}/t_{\text{ff}}$)	4	4
$\S\S \sigma_u, \sigma_h, \sigma_w$	0.3	0.3
$T_{\text{med},V}^{(u)}$	$1.5 \times 10^6 \text{ K}$	-
$T_{\text{med},V}^{(h)}$	$1.5 \times 10^6 \text{ K}$	-
$T_{\text{med},V}^{(w)}$	$3 \times 10^5 \text{ K}$	$3 \times 10^5 \text{ K}$
Output Parameters	$\gamma = 1$	$\gamma = 5/3$
$\ddagger f_V^{(w)}$ [percent]	8.5 (IC), 2.8 (IB)	28.7 (IC), 38.6 (IB)
$M_{\text{CGM}}^{(h)}, M_{\text{CGM}}^{(w)}$ [M_{\odot}]	$7.9, 1.4 \times 10^{10}$	$2.5, 1.6 \times 10^{10}$

[†] r_{200} is the radius within which mean density of the dark matter halo is 200 times the critical density of the present Universe.

^{††} We use the metallicity profile shown in Fig. 3 of [FSM20](#).

^{§§} Temperature spread denoted as s in [FSM17](#).

[‡] Total volume fraction in the warm phase within the CGM.

the product of density and temperature within a phase is constant. This is an approximation of the thermodynamic state of the gas. In general, density and temperature are independent, and 2D PDFs (say in density and temperature) are necessary to describe the gas distribution (cf. section 3).

For a shell of volume V and mass M at a radius r , the volume fraction of gas in the temperature range $[T, T + dT]$ is $\mathcal{P}_V^{(u)}(T)dT = dV/V$, and the mass fraction is $\mathcal{P}_M^{(u)}(T)dT = dM/M$. The average density for the shell is $\langle \rho^{(u)} \rangle = M/V$ and $dM/dV = \rho^{(u)}$ is the gas density at radius r in the temperature range $[T, T + dT]$. Since $\rho^{(u)} = dM/dV = (M/V)\mathcal{P}_M^{(u)}(T)dT/(\mathcal{P}_V^{(u)}(T)dT)$, the unmodified mass-PDF $\mathcal{P}_M^{(u)}(T)$ is related to the volume PDF as,

$$\mathcal{P}_M^{(u)} = \frac{\rho^{(u)}}{\langle \rho^{(u)} \rangle} \mathcal{P}_V^{(u)} = \frac{\langle T^{(u)} \rangle_M}{T} \mathcal{P}_V^{(u)}, \quad (4)$$

where $\langle \rangle$ denotes volume-weighted average and $\langle \rangle_M$ denotes mass-weighted average. The middle expression in Eq. 4 relating the mass and volume PDF is generic for any thermodynamic process of the internal perturbations within a phase. However, the rightmost expression assumes that the perturbations within the unmodified gas are isobaric. This isobaric assumption implies $\rho^{(u)}(r)T^{(u)}(r) = \langle \rho^{(u)}(r)T^{(u)}(r) \rangle = \langle \rho^{(u)}(r) \rangle \langle T^{(u)} \rangle_M(r)$ and hence gives the rightmost expression in Eq. 4.

The leftmost and the rightmost expressions in Eq. 4 can be inte-

grated over all temperatures to obtain ¹

$$\langle T^{(u)} \rangle_M^{-1} = \left\langle \frac{1}{T^{(u)}} \right\rangle = T_{\text{med},V}^{(u)-1} \int dx e^{-x} \mathcal{N}(x, \sigma_u),$$

where we use $T = T_{\text{med},V} e^x$. Further, on using the square completion given by Eq. 5 in the footnote, the RHS of the preceding expression can be simplified to

$$T_{\text{med},V}^{(u)-1} e^{\sigma_u^2/2} \int dx \mathcal{N}(x, -\sigma_u^2, \sigma_u),$$

relating the volume PDF and the mass-weighted average temperature as

$$\langle T^{(u)} \rangle_M = e^{-\sigma_u^2/2} T_{\text{med},V}^{(u)}. \quad (6)$$

Consistent with the isobaric assumption introduced earlier, we obtain the mass PDF by combining Eqs. 4 and 6 (and using Eq. 5),

$$\mathcal{P}_M^{(u)}(T) = \frac{1}{T} \exp \left[- \left(x + \frac{\sigma_u^2}{2} \right) \right] \mathcal{N}(x, \sigma_u) = \frac{1}{T} \mathcal{N}(y, \sigma_u), \quad (7)$$

where $y = x + \sigma_u^2/2$, $y \equiv \ln(T/T_{\text{med},M}^{(u)})$, and $T_{\text{med},M}^{(u)} = e^{-\sigma_u^2/2} T_{\text{med},V}^{(u)}$. This is similar to Eq. 2 and is applicable only under the isobaric assumption.

(iii) *Modifying the unmodified PDFs:* [FSM17](#) modifies the unmodified distribution of gas at every radius to incorporate the effects of physical processes such as radiative cooling. [FSM17](#) model considers two temperature phases, namely hot and warm, around which the temperature distribution is log-normal. Further, the assumption is that the coolest/densest unmodified gas at any radius, with the ratio of the cooling time to the free-fall time $t_{\text{cool}}/t_{\text{ff}}$ smaller than a threshold value (chosen to be 4 here), cools isochorically to the warm phase. The cooling time is $t_{\text{cool}} = (\gamma - 1)^{-1} p/n_H^2 \Lambda[T]$ and the free-fall time is $t_{\text{ff}} = \sqrt{2r/g[r]}$, where p is gas thermal pressure, n_H is the hydrogen number density, $\Lambda[T]$ is the cooling function, r is the shell radius and $g[r]$ is the gravitational acceleration. This model for the dropout of warm gas from the hot atmosphere is motivated by simulations of thermal instability in gravitationally stratified atmospheres (e.g., [Choudhury et al. 2019](#)). However, the warm gas is assumed not to cool further. The choice of the $t_{\text{cool}}/t_{\text{ff}}$ threshold determines the cut-off temperature T_c below which the hot gas is assumed to be thermally unstable, and the cooling to the warm phase is assumed to be isochoric. Isochoric cooling preserves the area under the curve of the unmodified PDF undergoing modification (see Fig. 2 for a cartoon and cyan dashed line in Fig. 3).

The volume fraction of the warm phase at any distance r from the halo center is

$$f_V^{(w)} = \int_{-\infty}^{x_c} dx \mathcal{N}(x, \sigma_u) = \frac{1}{2} \left[1 + \text{erf} \left(\frac{x_c}{\sqrt{2}\sigma_u} \right) \right], \quad (8)$$

where $x_c = \ln(T_c/T_{\text{med},V}^{(u)})$ corresponds to the temperature T_c below which the unmodified gas cools to produce the warm phase, and we

¹ We use the notation $\mathcal{N}(x, \mu, \sigma)$ for a normal distribution with mean μ and standard deviation σ . With only two arguments, $\mathcal{N}(x, \sigma)$ stands for a normal distribution with zero mean. Here and elsewhere, we complete the square in expressions to write the product of an exponential and a Gaussian as algebraically convenient shifted Gaussian in the following form,

$$e^{ax} \mathcal{N}(x, \mu, \sigma) = e^{a(\mu + a\sigma^2/2)} \mathcal{N}(x, \mu + a\sigma^2, \sigma). \quad (5)$$

have introduced the integral of a normal distribution,

$$\text{erf}(x) = \frac{2}{\sqrt{\pi}} \int_0^x dt e^{-t^2}.$$

Similarly, the mass fraction of the warm gas is

$$f_M^{(w)} = \int_{-\infty}^{y_c} dy \mathcal{N}(y, \sigma_u) = \frac{1}{2} \left[1 + \text{erf} \left(\frac{y_c}{\sqrt{2}\sigma_u} \right) \right], \quad (9)$$

where $y_c = x_c + \sigma_u^2 = \ln(T_c/T_{\text{med},M}^{(u)})$ corresponds to the cut-off temperature T_c . Note that $y_c > x_c$ implies $f_M^{(w)} > f_V^{(w)}$ (compare Eqs. 8 & 9), which is expected since the warm gas is denser.

Now, we need to decide the thermodynamic condition of the re-distributed gas. The warm phase is assumed to attain a new log-normal distribution about a specified median temperature $T_{\text{med},V}^{(w)}$ (see the vertical blue dotted line in Fig. 3). Since the warm phase has a short cooling time, it is assumed to be maintained in a steady state, at $T_{\text{med},V}^{(w)}$ by heating due to feedback and/or turbulent mixing. The warm gas volume distribution at any radius r is given by

$$\mathcal{P}_V^{(w)}(T) = \frac{f_V^{(w)}}{T} \mathcal{N}(x, \sigma_w), \quad (10)$$

where $x \equiv \ln(T/T_{\text{med},V}^{(w)})$, $T_{\text{med},V}^{(w)}$ is the median temperature of the warm gas, and $\mathcal{N}(x, \sigma_w)$ is the Gaussian distribution with standard deviation σ_w (see Eq. 3). Similarly, the mass-PDF for the warm gas is given by

$$\mathcal{P}_M^{(w)}(T) = \frac{f_M^{(w)}}{T} \mathcal{N}(y, \sigma_w),$$

where $y = x + \sigma_w^2$, $y \equiv \ln(T/T_{\text{med},M}^{(w)})$, and $T_{\text{med},M}^{(w)} = e^{-\sigma_w^2} T_{\text{med},V}^{(w)}$. Note that these expressions are analogous to unmodified PDFs (Eqs. 2 to 7) since the underlying PDF is the same, namely log-normal.

The modified hot phase is assumed to maintain the unmodified PDF above the cutoff temperature and is given by

$$\mathcal{P}_V^{(h)}(T) = \frac{1}{T} \mathcal{N}(x, \sigma_u) \mathcal{H}(x - x_c), \quad (11)$$

where x_c corresponds to the (radius dependent) cut-off temperature T_c and $\mathcal{H}(x)$ is the Heaviside function (unity for $x > 0$ and zero for $x < 0$).

(iv) *Local and global gas density*: It is useful to distinguish between the local and global average mass densities. We define the local gas density for a phase as $\langle \rho^{(i)} \rangle \equiv M^{(i)}/V^{(i)}$ (without subscript g in $\langle \rangle$; see Tab. 1 for notation) as the gas mass in phase i divided by the volume occupied by this phase. The global average gas density in phase i is $\langle \rho^{(i)} \rangle_g \equiv M^{(i)}/V$, defined as the gas mass in i th phase divided by the total volume $V = \Sigma V^{(i)}$ (Σ is sum over all phases). Thus, the local warm gas density is the *physical* density of the warm gas clumps.

The global average density of a phase corresponds to the same mass being spread uniformly over the whole volume V . To calculate observables like column densities, we assume that the cooler phases are uniformly spread throughout the volume in the form of a mist (Fig. 2(b); the same figure also shows other possibilities where the warm clouds do not uniformly fill the whole spherical shell). The reality is more complex than the mist limit which, by definition, gives an area-covering fraction of unity and is not consistent with observations. The warm/cool gas is likely to be spread in the form of clouds that occupy a small volume and cover a projected area

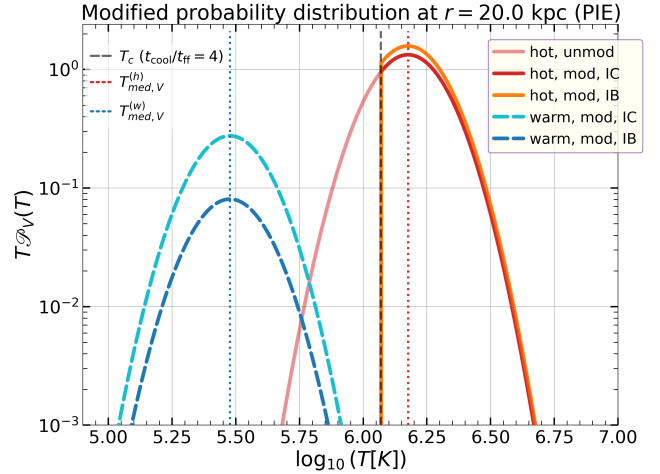


Figure 3. The volume probability distribution function (PDF) of temperature in a typical CGM shell at $r = 20$ kpc for a $\gamma = 1$ polytrope (isothermal FSM17 model). The *light red* curve shows the unmodified log-normal PDF of the hot phase about a median temperature $T_{\text{med},V}^{(h)} = 1.5 \times 10^6$ K (vertical red dotted line; see Eq. 6). The vertical *black* dashed line marks the temperature T_c where the cooling time to the free-fall time ratio $t_{\text{cool}}/t_{\text{ff}} = 4$ in this shell. Gas cooler than T_c is assumed to be thermally unstable and populates a new (internally-) isobaric distribution to form a warm phase about a median temperature $T_{\text{med},V}^{(w)} = 3 \times 10^5$ K (vertical blue dotted line). The *cyan* and *blue* dashed curves show the redistributed log-normal PDFs of the warm gas for isochoric and isobaric modification, respectively (see sections 2.1 & 2.3). Corresponding modified hot gas distributions are shown in *dark red* and *orange* curves. Being probability distributions, the sum of PDFs for warm and hot phases in both modifications (*red+cyan*: *isochoric*; *orange+blue*: *isobaric*) is normalized to unity.

fraction $\lesssim 1$ (e.g., panels a, c, d in Fig. 2). The CGM is expected to exhibit a patchy distribution of clouds with varying sizes and properties (also supported by cosmological simulations, e.g., Nelson et al. 2020). Consequently, different quasar sightlines probe a large variety of these cold and warm clouds, owing to the inherent stochasticity in their spatial distribution (see section 4.2 and also Hummels et al. 2023 for a comprehensive discussion).

For volume and mass fractions $f_V^{(i)}$ and $f_M^{(i)}$ respectively, the expressions for the local and global average gas densities in any phase i (where $i = h, w$) are given as

$$\langle \rho^{(i)} \rangle \equiv \frac{M^{(i)}}{V^{(i)}} = \frac{f_M^{(i)}}{f_V^{(i)}} \langle \rho^{(u)} \rangle \quad (12)$$

and

$$\langle \rho^{(i)} \rangle_g \equiv \frac{M^{(i)}}{V} = f_M^{(i)} \langle \rho^{(u)} \rangle, \quad (13)$$

where $f_V^{(w)} + f_V^{(h)} = f_M^{(w)} + f_M^{(h)} = 1$. Since each phase is assumed internally isobaric, we can define the density in the temperature range $[T, T + dT]$ as $\rho^{(i)} = \langle \rho^{(i)} \rangle \langle T^{(i)} \rangle_M / T$. The ratio of Eqs. 12 and 13 gives,

$$\langle \rho^{(i)} \rangle_g = f_V^{(i)} \langle \rho^{(i)} \rangle, \quad (14)$$

i.e., the global average density of a phase equals the product of the volume fraction and the local average density of that phase.

The solid lines in the left panel of Fig. 4 show the average global and local density profiles for the hot and warm phases for the isothermal CGM ($\gamma = 1$ polytrope) from which warm gas condenses iso-

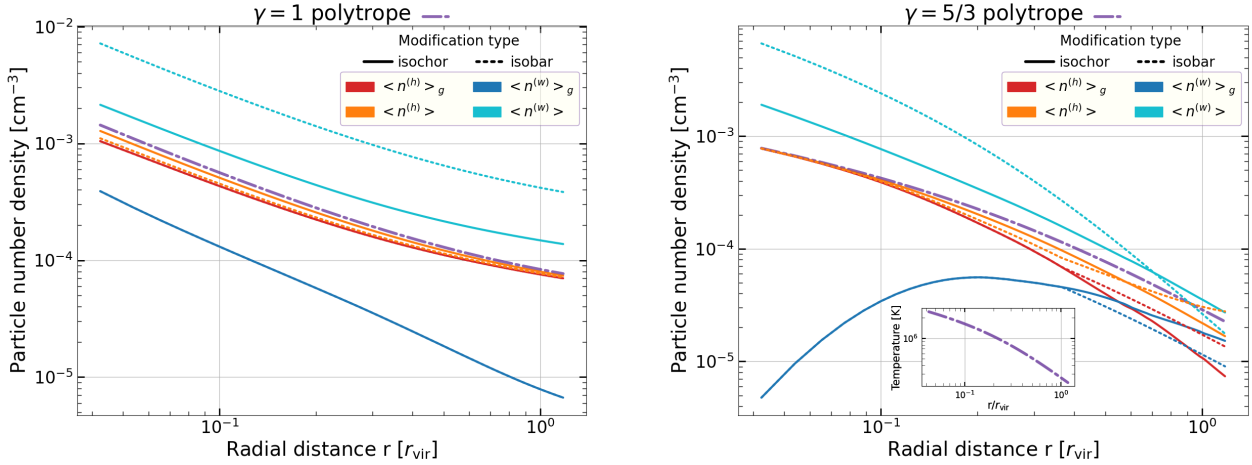


Figure 4. The different number density profiles for our isothermal ($\gamma = 1$ polytrope following [FSM17](#); *left panel*) and isentropic ($\gamma = 5/3$ polytrope following [FSM20](#); *right panel*) CGM models (see section 2.1 & 2.2). The purple dot-dashed lines in both panels show the unmodified profiles. Additionally, the inset in the right panel shows the unmodified temperature profile; the median unmodified temperature for the isothermal model (left panel) is 1.5×10^6 K. The solid lines show density profiles with isochoric redistribution of the warm phase while isobaric redistribution is shown using dashed lines. The global average density profiles (indicated by $\langle \rangle_g$) are shown in red and blue, whereas the local average density profiles (indicated by $\langle \rangle$) are shown in orange and cyan (see point (iv) in section 2.1 for the definitions of local and global average densities). The average global density profile for the warm phase in the right panel shows a dip towards the center because $t_{\text{cool}}/t_{\text{ff}}$ is larger there and only a small amount of unmodified gas lies below our chosen $t_{\text{cool}}/t_{\text{ff}} = 4$ threshold. In both the panels, the global density profiles for *isochoric* (solid red + blue) and *isobaric* (dashed red + blue) modifications coincide because the mass in each phase is the same in these cases. For $r/r_{200} \gtrsim 0.25$ the temperature of the unmodified isentropic profile (right panel) approaches the chosen warm phase temperature $T_{\text{med},V}^{(w)} = 10^{5.5}$ K (see inset in the right panel). In this case, we assume that only a fraction ≤ 0.4 of the unmodified gas can condense into the warm phase. Such a high dropout fraction compared to the isothermal model explains the large variations in different densities at large radii in the isentropic model.

chorically. As expected, the local density in all cases is larger than the global one. The global warm gas density at large radii is smaller because $t_{\text{cool}}/t_{\text{ff}}$ is larger and a smaller amount of gas drops out to the warm phase according to our prescription. The global and local densities of the hot phase are similar because most of the shell volume is occupied by the hot phase. The right panel is for an isentropic CGM ($\gamma = 5/3$ polytrope) discussed later in section 2.2.

(v) *Calculating observables:* Having obtained the hot and warm gas temperature PDFs and their corresponding profiles, we can now calculate several observables such as OVI, OVII, OVIII, NV column densities, dispersion measure (DM), X-ray spectrum, and emission measure (EM). As calculating observables is independent of generating the model profiles, details on computing observables are postponed until section 2.4.

As a demonstration of our general description of the probabilistic CGM model, we now discuss specific modifications to the original [FSM17](#) model.

2.2 Isentropic unmodified profile

[FSM17](#) used an isothermal ($\approx 1.5 \times 10^6$ K; comparable to the halo virial temperature) unmodified profile for the hot volume-filling CGM of Milky Way. Observations indicate the presence of OVI and NV ions in the Milky Way CGM ([Werk et al. 2013](#); [Tumlinson et al. 2011b](#)). Since these ions exist at a lower temperature ($\sim 10^{5.5}$ K), a CGM at the virial temperature is too hot to host sufficient OVI ions. To get around this, [FSM17](#) proposed a thermal instability ansatz (discussed in section 2.1) to introduce an additional warm phase at $10^{5.5}$ K. This results in a CGM that can host OVI and NV columns consistent with the observations (see top panels of Fig. 5). On the other hand, [FSM20](#) proposed an isentropic model without a spread in temperature at any radius. In contrast to the modified

isothermal model, where every galactocentric distance hosts both the hot and warm phases, [FSM20](#) has a unique temperature at every radius. Such an isentropic atmosphere in hydrostatic equilibrium (with reasonable boundary conditions) results in a transition from hot to warm temperatures at large radii approaching the virial radius (see inset in the right panel of Fig. 4). This naturally produces a CGM that can host enough OVI and NV ions at large radii, in compliance with observations, without the necessity of introducing a separate warm phase (see Fig. 10 of [FSM20](#)).

As pointed out earlier, any reasonable unmodified profile can be modified based on some physical prescription. The isothermal model in [FSM17](#) (presented in section 2.1) or the isentropic model in [FSM20](#) are examples of such unmodified hydrostatic atmospheres. In this section, we modify the unmodified isentropic profile of [FSM20](#) below the $t_{\text{cool}}/t_{\text{ff}} = 4$ threshold and introduce a warm phase. This highlights the general applicability of the procedure described in section 2.1. Another possibility (which we do not explore further) is to choose an unmodified hydrostatic profile at the precipitation threshold (say with $t_{\text{cool}}/t_{\text{ff}} = 20$ everywhere; [Sharma et al. 2012b](#); [Voit 2019](#)) and modify gas below $t_{\text{cool}}/t_{\text{ff}} = 4$ to account for the condensation of the denser gas (as motivated by [Choudhury et al. 2019](#)).

The right panel of Fig. 4 shows the unmodified isentropic profile (purple dot-dashed line) and the global and local number density profiles for the modified hot and warm phases. The global warm gas density profile at the center shows a dip because only a small fraction of gas condenses, as $t_{\text{cool}}/t_{\text{ff}}$ at small radii is large. If we conserve the total shell volume and the mass of the warm gas condensing out, we expect the global densities for both isochoric and isobaric modification to be the same. However, note that the separation between the isochoric and isobaric modified density profiles for both the hot and warm phases at $r/r_{200} \gtrsim 0.3$ happens because we restrict

the mass fraction of the warm gas to $f_M^{(w)} \leq 0.4$. The motivation behind this choice is that hydrostatic equilibrium assumes that most mass is in the ‘hot’ volume-filling phase.² Once the dropout gas mass fraction exceeds this, we limit the dropout mass to this value.

2.3 Isobaric instead of isochoric cooling to warm phase

FSM17 creates the warm phase by cooling the unmodified PDF below a cutoff temperature and assumes that the cooling happens isochorically to the warm phase (which is internally isobaric). While cooling may happen isochorically at intermediate temperatures with cooling times shorter than the sound-crossing time across cooling clouds (e.g., see Fig. 8 in Mohapatra et al. 2022), the warm/cold clouds are expected to achieve pressure equilibrium after a few sound crossing times. In any case, it is a useful generalization to relax the isochoric assumption. The other extreme assumption is to assume that cooling from unmodified temperatures to the warm phase occurs isobarically. In this case, the warm gas will occupy a smaller volume and the hot phase pressure can drop because of adiabatic cooling (see Fig. 2(c) which shows the warm phase volume in panel (a) compressed to a smaller volume). This can cause compression and reduction in the volume of each shell in the absence of additional heating sources. Motivated by the importance of AGN/supernova feedback heating, the required additional heating of the hot phase is assumed to be present to preserve the shell volume.

Let $V^{(u)}$ be the volume of a spherical shell in the unmodified profile that we split into smaller volumes of hot and warm phases $V^{(h)}$ and $V^{(w)}$ respectively. Mass conservation gives, $\langle \rho^{(h)} \rangle V^{(h)} + \langle \rho^{(w)} \rangle V^{(w)} = \langle \rho^{(u)} \rangle V^{(u)}$ and pressure balance between phases implies $\langle \rho^{(h)} \rangle \langle T^{(h)} \rangle_M = \langle \rho^{(w)} \rangle \langle T^{(w)} \rangle_M = \langle \rho^{(u)} \rangle \langle T^{(u)} \rangle_M$. Now these are three equations for four unknowns, namely, $\langle \rho^{(h)} \rangle$, $\langle \rho^{(w)} \rangle$, $V^{(h)}$, $V^{(w)}$. The median temperatures $\langle T^{(h)} \rangle_M$ and $\langle T^{(w)} \rangle_M$ are known since we specify them to construct the hot and warm PDFs. Since the total volume remains unchanged and the total PdV work done for isobaric modification is zero, the total internal energy before and after modification remains the same; i.e., $\langle \rho^{(h)} \rangle \langle T^{(h)} \rangle_M V^{(h)} + \langle \rho^{(w)} \rangle \langle T^{(w)} \rangle_M V^{(w)} = \langle \rho^{(u)} \rangle \langle T^{(u)} \rangle_M V^{(u)}$. Thus, we can uniquely determine our modified hot and warm gas profiles. In this ansatz, energy loss due to the cooling of the hot phase to form the warm gas needs to be exactly compensated by external heating sources (which can come from feedback heating) to prevent compression of the hot phase. This is similar to the global thermal balance ansatz used in the modeling of cool core clusters (e.g., Sharma et al. 2012a).

The mass fraction in the warm phase $f_M^{(w)}$ is the same as for isochoric cooling to the warm phase, given by Eq. 9 (since the same mass cools to the warm phase under both isochoric and isobaric assumptions). But this warm phase occupies a smaller volume under isobaric assumption compared to isochoric. The average warm gas density is, $\langle \rho^{(w)} \rangle = \langle \rho^{(u)} \rangle \langle T^{(u)} \rangle_M / \langle T^{(w)} \rangle_M$ since the warm phase and the unmodified gas have the same pressure. Thus, the warm phase volume fraction for this case is given by

$$f_V^{(w)} = \frac{V^{(w)}}{V} = \frac{M^{(w)}}{\langle \rho^{(w)} \rangle} \frac{\langle \rho^{(u)} \rangle}{M^{(u)}} = \frac{\langle T^{(w)} \rangle_M}{\langle T^{(u)} \rangle_M} f_M^{(w)}. \quad (15)$$

Recall that $\langle T^{(w)} \rangle_M / \langle T^{(u)} \rangle_M = T_{\text{med},V}^{(w)} e^{-(\sigma_w^2 - \sigma_u^2)/2} / T_{\text{med},V}^{(u)}$

(see Eq. 6). Fig. 4 shows that the local number density is higher for isobaric modification as compared to isochoric. However, since the mass of gas in all phases for both models is identical, the global densities are also, therefore, identical (shell volume is constant). The volume (and also the area if not all sightlines are covered by clouds) filling factor for the isobaric warm phase is expected to be smaller than the isochoric case. While the column densities for isobaric and isochoric modifications are similar (see Fig. 5), the EM and luminosity are expected to be higher for isobaric modification because of a higher density in this case.

2.4 Generating observables from probabilistic CGM models

Most of the observables are line-of-sight (LOS) integrals of various physical quantities. For example, column density is $\int n ds$ where n is the local number density of a particular ion, and ds is an infinitesimal path length along the LOS. Similarly, EM is proportional to $\int n^2 ds$. In our probabilistic model, every shell of the CGM is multiphase, and each phase contributes to these LOS integrals. We first discuss the column density estimate from our probabilistic model. Carrying this forward to other LOS integrals is straightforward.

2.4.1 Column density in absorption

The contribution by phase i in the temperature range $[T, T + dT]$ to the LOS integral is $\int n^{(i)} ds^{(i)}$, where $ds^{(i)}$ is the path length through phase i . Assuming clouds to be uniformly spread throughout the shell, i.e., the mist limit, implies $dV^{(i)} = dA_{\perp} ds^{(i)}$ and $ds^{(i)} = dV^{(i)} / V$ (see Tab. 1 for notation), where dA_{\perp} is an infinitesimal area perpendicular to the LOS and $dV^{(i)}$ is the differential volume of phase i . The column density is $\int n^{(i)} ds^{(i)} = \int ds \int n^{(i)} dV^{(i)} / V = \int ds \int n^{(i)} \mathcal{P}_V^{(i)}(T) dT$, where the last expression follows from the definition of volume PDF. Note that $n^{(i)}$ is the local density of phase i and, in general, $n^{(i)}$ depends on (n, T) , i.e., the thermodynamic state assumed within the phase. The expression for column density can be simplified further using the global average density of a particular phase i , i.e., $\langle n^{(i)} \rangle_g = \int n^{(i)} \mathcal{P}_V^{(i)}(T) dT$. Thus, the column density in the mist limit from all the phases can be written as $\Sigma \int \langle n^{(i)} \rangle_g ds$. The global number density is appropriate here because only a fraction of the available volume is occupied by the gas in a given phase. Similar expressions can be obtained for other LOS integrals.

Specifically, the expression for the column density of OVI at an impact parameter b is

$$N_{\text{OVI}}(b) = \int \langle n_{\text{OVI}} \rangle_g(s) ds = 2 \int_b^{r_{\text{CGM}}} \frac{\langle n_{\text{OVI}} \rangle_g(r) r dr}{\sqrt{r^2 - b^2}}, \quad (16)$$

where $\langle n_{\text{OVI}} \rangle_g$ is the global density of OVI ion in a shell at radius r , as motivated in the previous paragraphs. The modified PDF and the global densities of the different gas phases can be used to estimate the global number density profiles of different ions (this assumes that all phases are uniformly mixed at each radius, also known as the mist approximation; see Fig. 2b). The global average number density of OVI (to be plugged in Eq. 16) as a function of radius r is given by (assuming photo+collisional ionization equilibrium; PIE) the following expression,

$$\langle n_{\text{OVI}} \rangle_g(r) = a_{\text{O}} \left(\frac{Z(r)}{Z_{\odot}} \right) \left[I^{(w)} + I^{(h)} \right], \quad (17)$$

² This choice, although somewhat arbitrary, should not affect the observables because of the comparable ‘warm’ and ‘hot’ phase temperatures at these radii.

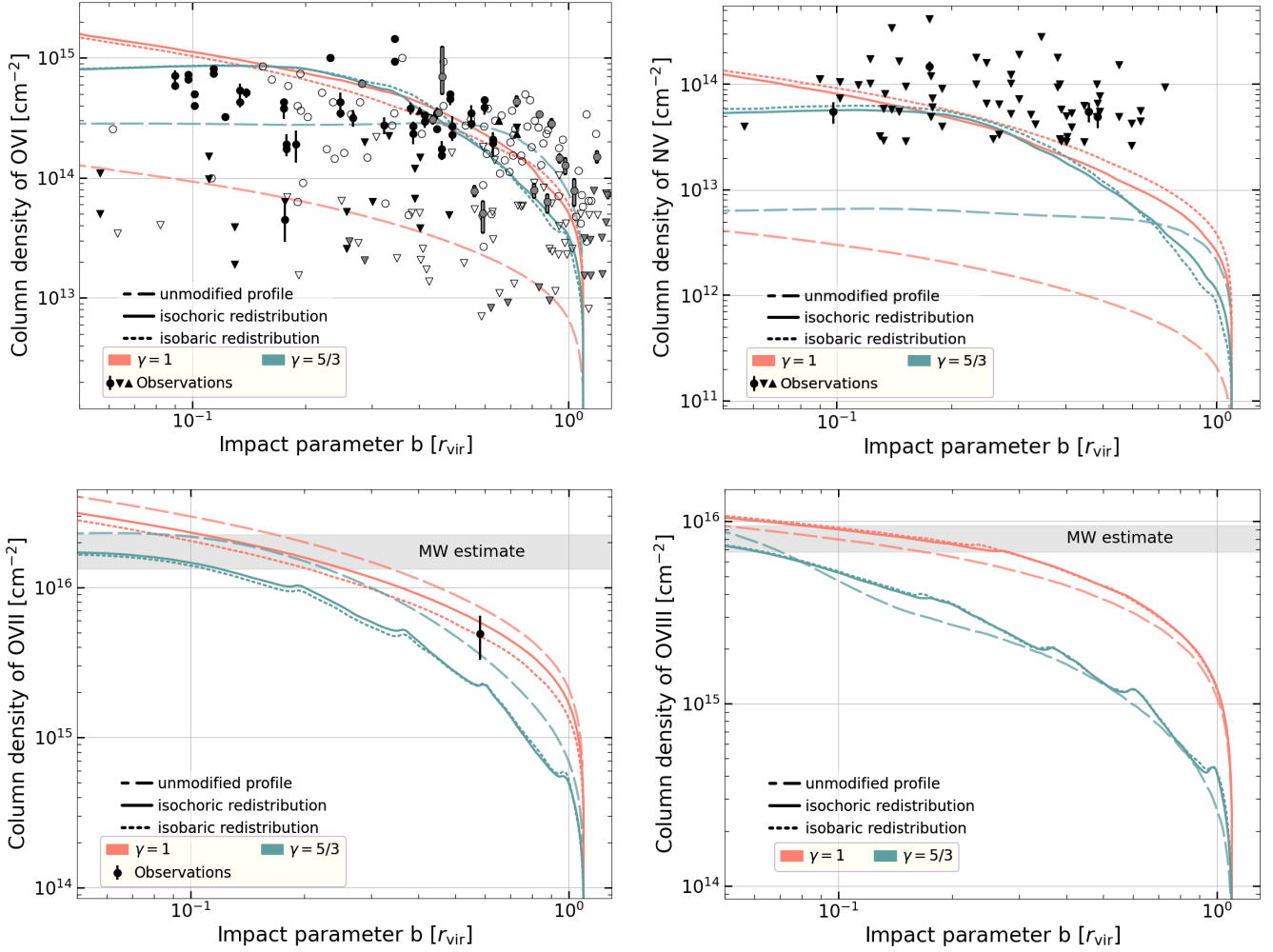


Figure 5. The column density of different ions as a function of the impact parameter (normalized by the virial radius) from our isothermal ($\gamma = 1$ polytrope) and isentropic ($\gamma = 5/3$ polytrope) models (see Fig. 4 for density profiles). In all the panels, the solid lines refer to isochoric modification, while the isobaric modification is shown using the dotted lines. Using the dashed lines, we also show the column density estimates generated from the unmodified (isothermal and isentropic) profiles for reference. *Orange* lines are for the isothermal model and *cyan* for isentropic. *Top panels:* The column densities of ions tracing the warm phase, OVI on the left and NV on the right. The data points are inferred from absorption spectra of quasar sightlines through external galaxies (OVI: COS-Halos [Tumlinson et al. 2011a; Werk et al. 2016] and eCGM surveys [Johnson et al. 2015] in solid black markers, CGM² survey [Tchernyshyov et al. 2022] in open black markers, and CUBS VII survey [Qu et al. 2024] in solid gray markers; and NV: Werk et al. 2013 in solid black markers). The (inverted)-triangles are (upper)-lower limits. *Bottom panels:* The column densities of ions tracing the hot phase, OVII on the left and OVIII on the right. The lone observation data point for OVII for an external galaxy is from Mathur et al. 2023 (cf. sections 2.1 & 3.1 in their paper), which also produces OVIII column density of $7.8 \pm 2.6 \times 10^{15} \text{ cm}^{-2}$ (not marked; private communication, Sanskriti Das). Due to limited observations for external galaxies, we only indicate the range estimated from the Milky Way CGM for the OVII and OVIII columns (in gray bands; from *Chandra* observations by Gupta et al. 2012 and *XMM-Newton* observations by Fang et al. 2015; Das et al. 2019a). Since the sun is only 8 kpc from the Galactic center, the column densities for the Milky Way ($\times 2$; shown in gray bands) provide an estimate on the upper limit of the ion columns in Milky Way-like external galaxies.

where

$$\mathcal{I}^{(i)} = \int dT \left(\frac{\mu^{(i)}}{\mu_H^{(i)}} \right) n^{(i)} \mathcal{P}_V^{(i)}(T) f_{\text{OVI}}(n^{(i)}, T),$$

for each component, where $\mu^{(i)}$ depends on $n^{(i)}$ and T , a_O is the number ratio of oxygen to hydrogen atoms in the sun (Asplund et al. 2009), $Z(r)$ is the CGM metallicity (metal mass to total gas mass ratio) at that radius, and f_{OVI} is the OVI ion fraction. We can use the equation of state $n^{(i)} T = \langle n^{(i)} \rangle \langle T^{(i)} \rangle_M$ to calculate the temperature integral above (since we assume the phases to be internally isobaric). We adopt the metallicity profile introduced by FSM20 (see their Eqs. 8 & 9). Our model parameters are listed in

Tab. 2. We stick to FSM17 parameter values since we wish to test how models tuned for a particular observable fare against a broader range of multi-wavelength observables. Further, the observables are estimated considering the mist limit, which gives a covering fraction of unity (see discussion at point (iv) in section 2.1 for details). It is anticipated that the measured column densities will exceed our mist limit estimates because of the discrete nature of the clouds (discussed further in section 4.2) and the ease of detecting higher columns.

The top panels of Fig. 5 show the OVI and NV column density profiles from our isothermal ($\gamma = 1$) model as a function of the impact parameter. These ions trace the warm $\sim 10^{5.5} \text{ K}$ phase (e.g., see Fig. 6 in Tumlinson et al. 2017). The observational data

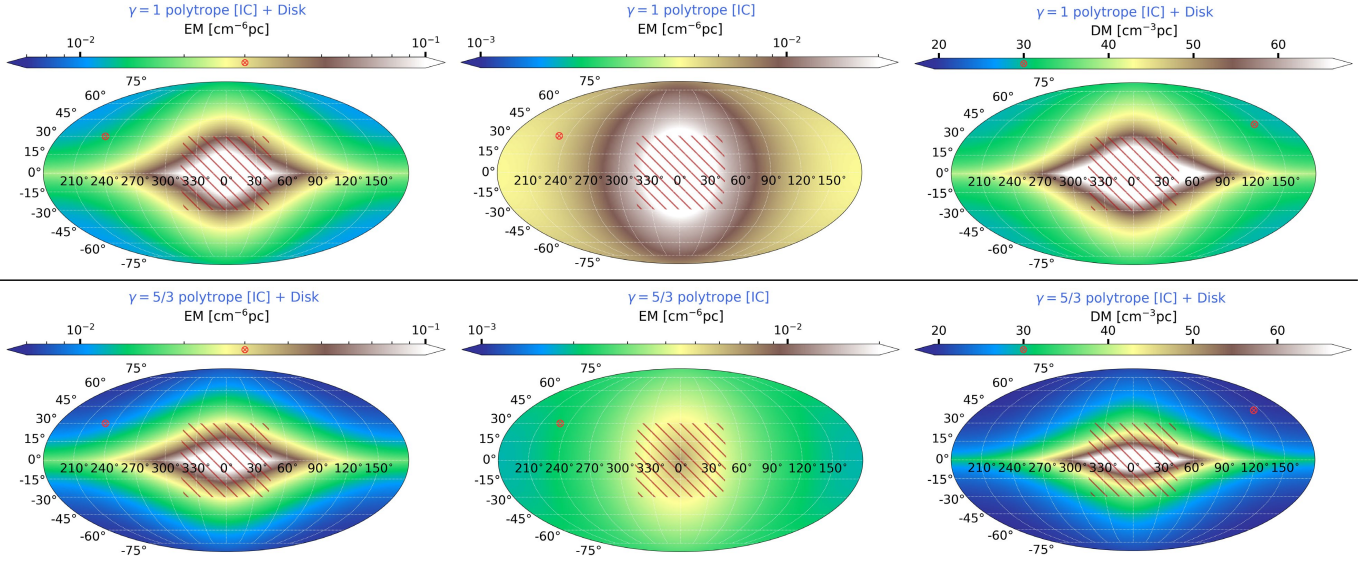


Figure 6. The Mollweide maps of observables in Galactic coordinates (l, b) from our models (namely, $\gamma = 1$ [upper panels] and $\gamma = 5/3$ [lower panels] polytropes with isochoric modification). The *left* and *middle* columns display our modeled Milky Way emission measure, with and without a coronal disk respectively, as observed from the position of the solar system. The *right* column shows the corresponding dispersion measure. These maps are generated from different CGM models discussed in section 2 (gas profiles shown in Fig. 4). Eq. 19 models the coronal disk component. The *red crosshair* in the EM maps marks the eFEDS sightline ($l, b \approx 230^\circ, 30^\circ$) observed by Pontì et al. 2023b and the estimated EM is $2.937 \times 10^{-2} \text{ pc cm}^{-6}$. The *red crosshair* in the DM maps in the *right* column marks the sightline ($l, b = 142.19^\circ, 41.22^\circ$) of a nearby FRB, in the M81 galaxy (Bhardwaj et al. 2021). The DM estimated for the Milky Way halo along this sightline is 30 pc cm^{-3} . The region near the Galactic center is hatched in the maps to indicate that predictions would be unreliable there. This area is contaminated by eROSITA bubbles (Predehl et al. 2020) and other features, as well as the central cusp in the number density profile (Fig. 4).

are taken from Werk et al. 2013, 2016; Tchernyshyov et al. 2022 & Qu et al. 2024. The virial radii of the galaxies from the COS-Halos survey used in the normalization of the impact parameter are taken from Tumlinson et al. 2013. All the observed column densities were calculated from corresponding equivalent widths of ionic transitions in the absorption spectra using either Apparent Optical Depth analysis (Savage & Sembach 1991) or Voigt profile fitting (e.g. Carswell & Webb 2014; also see references from the corresponding surveys). Throughout this work, for the ionization models, we use CLOUDY 2017 (Ferland et al. 2017) and consider the CGM to be in photo+collisional ionization equilibrium (PIE) in the presence of Haardt-Madau extragalactic UV radiation (Haardt & Madau 2012) at a redshift of 0.2 (matching COS-Halos galaxies). For some ion levels, the differences between the collisional (CIE) and photo+collisional ionization equilibrium (PIE) can be significant (e.g., see Fig. 6 in FSM20 & discussion in Appendix C).

Similarly, the bottom panels show the OVII and OVIII column density profiles. These ions trace the hot ($\gtrsim 10^{5.5} \text{ K}$) gas, and presently virtually no constraints exist on their column densities in external galaxies, except for the one recent observation of OVII column by Mathur et al. 2023. Moreover, absorption/emission properties of ions like OVII may be significantly altered by resonant scattering (Nelson et al. 2023), not taken into account in our modeling. Observations also indicate that the absorption profiles of these ions can be highly saturated. For example, the ratio of equivalent widths for $K\alpha$ to $K\beta$ transition for OVII along multiple sightlines probing the Milky Way CGM deviates from a constant value expected (~ 0.15) in the optically thin regime (Gupta et al. 2012). The poor spectral resolution in X-rays does not allow precise Voigt profile fitting. For OVII, we use the column density range indicated in Tab. 2 of Gupta et al. (2012). From the OVIII equivalent width (EW) given in the same table, we obtain N_{OVIII} using the linear

relation between the equivalent width (EW) and column density in the optically thin regime. In the absence of adequate constraints from external galaxies for these high ionization states, we show the scaled OVII and OVIII columns of the Milky Way CGM (Gupta et al. 2012; Fang et al. 2015; Miller & Bregman 2015; Miller & Bregman 2013), which are indicated in gray bands.

To compare with our probabilistic models, in Fig. 5 we also show the column density profiles for the unmodified profiles using dashed lines (red: isothermal; blue: isentropic). The unmodified isentropic profile in FSM20 is cooler in the outskirts and can, therefore, produce higher OVI column density compared to the unmodified isothermal profile in FSM17. We modify the isentropic profile following the thermal instability ansatz in FSM17 with the threshold $t_{\text{cool}}/t_{\text{ff}} = 4$, and the warm phase has a median temperature of $10^{5.5} \text{ K}$. As expected, this modification does not significantly alter the column density profiles of OVI in the isentropic model. Since the unmodified isentropic profiles are cooler at large radii, the OVII and OVIII column densities are smaller farther out than for the isothermal model (see bottom rows of Fig. 5).

2.4.2 Emission & Dispersion measures

Just like the individual ions, we can calculate the electron number density to determine the dispersion and emission measures produced by our CGM model. For every sightline (l, b) in the Mollweide maps in Fig. 6, we sample 1000 points along the line of sight (uniformly spaced from the location of the sun till r_{CGM}). For each of these points, we calculate the (r, θ, ϕ) coordinates from the Galactic center and calculate the desired observable quantity interpolated from our models. These values are then numerically integrated to obtain the observables at each (l, b) . These observables can alternatively be (numerically) integrated directly in terms of

the Galactocentric distance r , employing a change of variables as discussed in Appendix B (Eq. B6).

In the mist approximation, the contribution by a given phase to the emission measure integral $\int (n^{(i)})^2 ds^{(i)} = \int \langle (n^{(i)})^2 \rangle_g ds$, with

$$\langle (n^{(i)})^2 \rangle_g = \int \left(\frac{\rho^{(i)}}{\mu_i m_p} \right)^2 \mathcal{P}_V^{(i)}(T) dT,$$

where $\rho^{(i)}$ can be related to T by the assumed thermodynamic equation of state within the phase (isobaric in our case). Note that the ratio of emission measure and the square of column density contributed by a uniform volume is the clumping factor³

$$C = \frac{\Sigma \langle (n^{(i)})^2 \rangle_g}{[\Sigma \langle n^{(i)} \rangle_g]^2}. \quad (18)$$

Since the ionization of hydrogen and helium is the dominant contributor of free electrons, the dispersion measure ($DM = \int n_e ds$) is mostly insensitive to the ionization state of the metals. This makes DM-based inferences robust and less sensitive to model parameters. The DM generated from our models can be compared with the DMs of the Fast Radio Bursts (FRBs) in nearby galaxies (Bhardwaj et al. 2021; Ravi et al. 2023; Cook et al. 2023). The emission measure $EM = \int n_e n_H ds$ is another observable that we generate from our CGM models. The EM constraints are available from the observations of the continuum soft X-ray emission from the Milky Way CGM. Estimating EM requires the observed X-ray spectrum to be broken down into contributions from several components like the local hot bubble, cosmic X-ray background, solar wind charge exchange, MW halo, and MW Galactic disk. Many different surveys, till now, have estimated the EM from the Milky Way, e.g., *ROSAT* (Hirth et al. 1992), *Suzaku* (Gupta et al. 2014), *XMM-Newton* (Hensley & Shelton 2010, 2013; Das et al. 2019b; Bhattacharyya et al. 2023), *HaloSat* (Kaaret et al. 2019, 2020; Bluem et al. 2022), and *eROSITA* eFEDS (Ponti et al. 2023a,b). We compare our models with these observations.

The EM value with just the spherical CGM (middle panels of Fig. 6) is of a few factors smaller than the value observed in the eFEDS field. Thus, we include an X-ray emitting disk adapted from (Yamasaki & Totani 2020) having a density

$$n_H(R, z) = n_{H,0} \exp \left[- \left(\frac{R}{R_0} + \frac{|z|}{z_0} \right) \right], \quad (19)$$

where $n_{H,0}$ is the hydrogen number density at the center of the coronal disk and $R_0 = 8.5$ kpc and $z_0 = 3.0$ kpc are the scale radius and height of the disk. We set $n_{H,0} = 4.8 \times 10^{-3} \text{ cm}^{-3}$ and assume the disk to be isothermal at a temperature of 1.5×10^6 K. Our parameter values are different from Yamasaki & Totani 2020, adjusted to match the recently observed X-ray surface brightness of the CGM in the eFEDS field (Ponti et al. 2023b). Simulations and theoretical considerations suggest that this coronal disk is expected and is maintained by heating from supernovae-driven outflows (Weiner et al. 2009; Rubin et al. 2010), which form the rising part of the Galactic fountain (Bregman 1980; Crain et al. 2010; Fraternali 2017; Kim & Ostriker 2018; Grand et al. 2019). A coronal disk not only increases the X-ray surface brightness towards the eFEDS field but also increases its anisotropy towards and opposite to the Galactic center, which can be compared with observations (e.g., Fig. 6 in

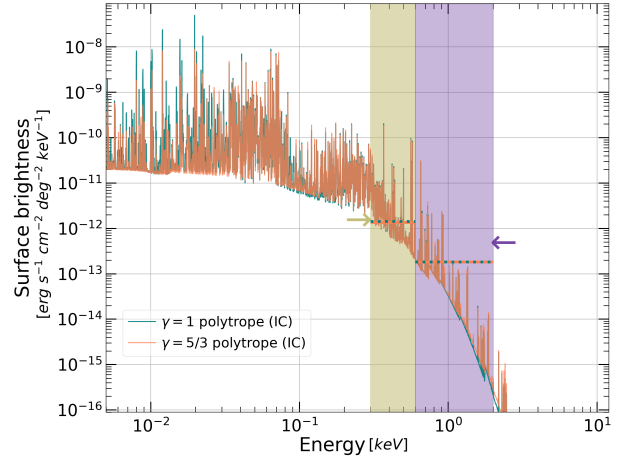


Figure 7. Synthetic surface brightness along $l, b = 230^\circ, 30^\circ$ (eFEDS region) from our polytropic models of the CGM (see Fig. 4 and section 2 for details). The cyan curve is for a $\gamma = 1$ polytrope while the orange curve is for $\gamma = 5/3$ polytrope, both of which consider isochoric modifications. The vertical olive (0.3 – 0.6 keV) and purple (0.6 – 2.0 keV) bands mark the energy bands used for the eFEDS survey of the Milky Way CGM in soft X-rays (Ponti et al. 2023b). The observed surface brightness towards the eFEDS field of the CGM in 0.3 – 2 keV is $2.05 \times 10^{-12} \text{ erg cm}^{-2} \text{ s}^{-1} \text{ deg}^{-2}$ (Tab. 4 in Ponti et al. 2023b). The surface brightness in the same energy band (0.3 – 2.0 keV) obtained from $\gamma = 1$ and $\gamma = 5/3$ polytrope models with the addition of a coronal disk (see Eq. 19) is 1.07×10^{-12} and $9.4 \times 10^{-13} \text{ erg cm}^{-2} \text{ s}^{-1} \text{ deg}^{-2}$, respectively. The arrows indicate the surface brightness levels observed in each band, while the horizontal lines show the model prediction.

Bluem et al. 2022).⁴ We assume that the contribution from the disk (modeled by Eq. 19) can simply be superimposed for all the observables.

The top row of Fig. 6 shows the EM and DM maps in Mollweide projection for our isochorically modified isothermal ($\gamma = 1$ polytrope) CGM model, while the bottom row shows the EM and DM maps for isochorically modified isentropic ($\gamma = 5/3$ polytrope) CGM model (see section 2.2). The middle column shows the EM maps without the disk to highlight the CGM contribution for the $\gamma = 1$ and the $\gamma = 5/3$ polytropes. Because of a higher density at larger radii in the isothermal model, the isothermal model has higher values of EM and DM (see Fig. 4). The red crosshairs on these maps mark the observed sightlines. Along $l, b \approx 230^\circ, 30^\circ$, Ponti et al. 2023b (the eFEDS survey) report the Milky Way EM to be $2.9 - 3.1 \times 10^{-2} \text{ pc cm}^{-6}$ (their Tab. 2). Along $l, b = 142.19^\circ, 41.22^\circ$, Bhardwaj et al. 2021 estimate the DM of the Milky Way (using a nearby FRB in the M81 galaxy) to be 30 pc cm^{-3} . The isothermal models exhibit better agreement with the observed EM and DM values, as shown quantitatively in Tab. 4. The model EM values, dominated by the disk, are smaller by a factor of 2-3 than observations (perhaps due to additional ISM contribution along this sightline). The DM values, dominated by the spherical CGM, are in very good agreement. Because of a weaker sensitivity to the dense ISM, the DM is a more constraining probe of the CGM than EM.

³ Clumping factor quantifies the spread in density, considered here in the misty limit. Note that multiphase CGM is both clumpy (showing spread in density) and patchy/cloudy (not filling the volume uniformly), and these two are distinct properties.

⁴ We note that the CGM emission measure estimated in Ponti et al. (2023b) is larger than in Bluem et al. (2022) mainly because the former estimates the CGM metallicity to be $\lesssim 0.1 Z_\odot$ from the data. In contrast, the latter assumes the standard value of $0.3 Z_\odot$.

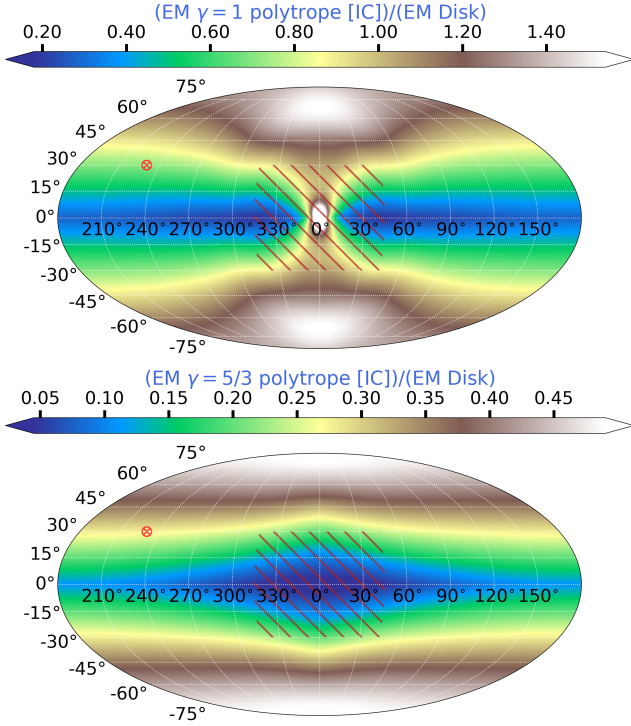


Figure 8. Mollweide projection in Galactic coordinates (l, b) of the ratio of CGM halo to disk emission measure (EM) for $\gamma = 1$ (top panel) and $\gamma = 5/3$ (bottom panel) polytropes, both with isochoric modification. The red crosshair marks the eFEDS sightline $l, b = 230^\circ, 30^\circ$. Along this sightline, the halo to disk EM is ≈ 0.7 and 0.25 for the $\gamma = 1$ and the $\gamma = 5/3$ polytropes, respectively. The neighborhood of the Galactic center is again hatched (like 6) due to possible contamination by the eROSITA bubble. In the $\gamma = 1$ map, the CGM dominates towards the Galactic center because of the cusp-like density profile in this case (see left panel of Fig. 4).

Recently, the *eROSITA* X-ray telescope has looked at an unobscured field to constrain the Milky Way CGM properties. The two X-ray bands in the *eROSITA* eFEDS survey outlined by Pontì et al. 2023b are $0.3 - 0.6$ keV and $0.6 - 2.0$ keV. Fig. 7 shows the emission spectrum from our isothermal ($\gamma = 1$ polytrope) and isentropic ($\gamma = 5/3$ polytrope; see section 2.2) models, both with isochoric modification. The surface brightness is calculated towards the direction of the eFEDS field ($l, b \equiv (230^\circ, 30^\circ)$). The two models give very similar surface brightness spectra because they are dominated by the coronal disk component, which is the same in both cases. The observed X-ray surface brightness in $0.6-2$ keV is twice our model predictions because of ISM/CGM clouds along the sightline and an even hotter/super-virial coronal disk component, as suggested by recent observations (Pontì et al. 2023b; Bluem et al. 2022). If needed, such a component can be added to our models, as described in section 3.

Fig. 8 maps out the ratio of EM contributed by the spherical CGM component to the disk for both the isothermal and isentropic models. As expected, the spherical component dominates at high latitudes ($b \gtrsim 30^\circ$). All sky maps from eROSITA at high latitudes and away from the Galactic center can help us distinguish between different CGM+disk models.

3 MORE THAN TWO PHASES

Observations and numerical simulations show that in addition to the volume-filling hot phase ($\sim 10^6$ K) and the intermediate warm phase ($\sim 10^5$ K), there is a cold ($\sim 10^4$ K) phase in the CGM. The hot and warm phases presumably cool to produce the cold gas. Cold gas from the dense ISM can also be introduced into the CGM by supernovae/AGN-driven winds. Ram pressure stripping of satellite galaxies can deposit the satellite's cold gas into the CGM of the host galaxy (Rohr et al. 2023). Recent observations of many galaxies also seem to support this picture of three-phase gas distribution (Sameer et al. 2024).

Simulations show that the hot and cold phases have relatively narrow distributions in $\log T$ compared to a broader distribution of warm/intermediate phase (e.g., see the left panel of Fig. 6 in Nelson et al. 2020; middle panel of Fig. 5 in Kanjilal et al. 2021; Fig. 4 in Mohapatra et al. 2022). Similarly, there is a large spread in density for all phases. This motivates us to introduce 2D log-normal distributions (in ρ - T space) with appropriate spreads in ρ and T for each phase.

We introduce a uniform (one-zone) model for the CGM, where spatial variation is not considered for simplicity. Our formalism can be generalized to include variations with radius. We approximate the volume-PDF of the CGM to be the sum of a number of (three for specificity) 2D log-normal distributions centered at chosen median temperatures and densities. Namely (the summation indices are not explicitly mentioned later),

$$\begin{aligned} \mathcal{P}_V^{2D}(\rho, T) d\rho dT &= \sum_{i=h,w,c} \mathcal{P}_V^{2D(i)}(\rho, T) d\rho dT \\ &= \sum_{i=h,w,c} \mathcal{P}_V^{2D(i)}(x, y) dx dy \\ &= \sum_{i=h,w,c} f_V^{(i)} \mathcal{N}^{2D}(\mathbf{x}, \mathbf{x}_i, \Sigma_i) dx dy, \end{aligned} \quad (20)$$

where $x = \ln(\rho/\rho_{\text{med},V}^{(u)})$, $x_i = \ln(\rho_{\text{med},V}^{(i)}/\rho_{\text{med},V}^{(u)})$, $y = \ln(T/T_{\text{med},V}^{(u)})$, $y_i = \ln(T_{\text{med},V}^{(i)}/T_{\text{med},V}^{(u)})$, $\mathbf{x} = (x, y)$, $\mathbf{x}_i = (x_i, y_i)$, Σ_i is the $x - y$ covariance matrix of each phase, and $f_V^{(i)}$ is the volume fraction of each phase. Here $\rho_{\text{med},V}^{(i)}$ and $T_{\text{med},V}^{(i)}$ are the median density and temperatures of each phase and x_i, y_i are the medians in (x, y) space while $\rho_{\text{med},V}^{(u)}$, $T_{\text{med},V}^{(u)}$ are respectively the phase independent reference density, temperature for the volume-PDF. Note that the 2D volume-PDF \mathcal{P}_V^{2D} is log-normal in (ρ, T) but a 2D Gaussian in the (x, y) space. In the numerical implementation of our model, we used hydrogen number density n_H as an independent variable instead of ρ . The 2D rotated-Gaussians $\mathcal{N}^{2D}(\mathbf{x}, \mathbf{x}_i, \Sigma_i)$ are the 2D PDFs for each phase i in the $x - y$ plane, and their explicit expression is

$$\begin{aligned} \mathcal{N}^{2D}(\mathbf{x}, \mathbf{x}_i, \Sigma_i) &= \frac{1}{2\pi\sigma_{1,i}\sigma_{2,i}} \exp \left\{ - \left(A_i(x - x_i)^2 \right. \right. \\ &\quad \left. \left. + B_i(x - x_i)(y - y_i) + C_i(y - y_i)^2 \right) \right\}, \end{aligned} \quad (21)$$

where $A_i = (\cos^2 \alpha_i / \sigma_{1,i}^2 + \sin^2 \alpha_i / \sigma_{2,i}^2) / 2$, $B_i = \sin 2\alpha_i (1 / \sigma_{1,i}^2 - 1 / \sigma_{2,i}^2) / 2$, $C_i = (\sin^2 \alpha_i / \sigma_{1,i}^2 + \cos^2 \alpha_i / \sigma_{2,i}^2) / 2$ in terms of the standard deviations ($\sigma_{1,i}$, $\sigma_{2,i}$) along the principal axes of the individual Gaussians and the angle of rotation (α_i) relative to the x axis. Note that $4A_i C_i - B_i^2 = 1 / (\sigma_{1,i}^2 \sigma_{2,i}^2)$ is a useful simplification utilized later. Hence, the 2D volume-PDF can be fitted using the following parameters for each phase: median density $\rho_{\text{med},V}^{(i)}$, tem-

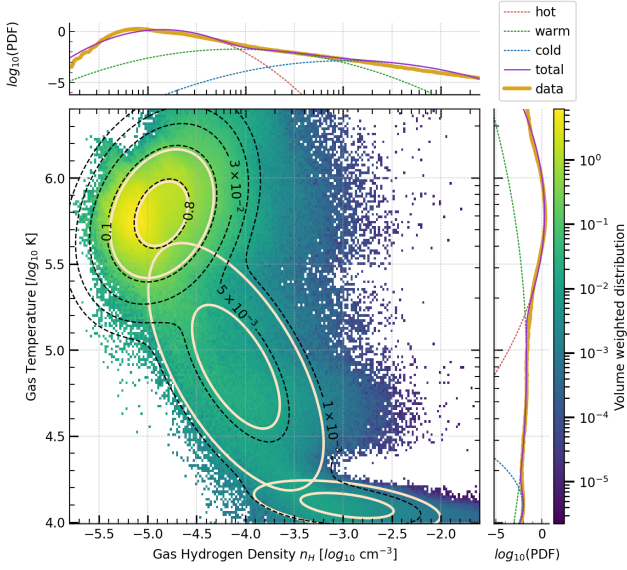


Figure 9. The central plot in this figure shows the volume-weighted 2D histogram of hydrogen number density and temperature of the CGM for our chosen halo from the Illustris TNG50-1 cosmological simulation (halo ID-110, snap-84; only ‘non-star forming’ gas within the virial radius is included). The white rotated ellipses indicate 1σ and 2σ contours for each phase (cold, warm, and hot) obtained by fitting Eq. 20 and the black dashed contours correspond to the total PDF including all phases. The top and right panels show the marginalized 1D PDFs in density and temperature, respectively. The thick solid line in yellow shows the marginalized PDFs from the simulation data. The thin solid lines in purple are from our best-fit model, with contributions from individual phases shown by dotted lines in colors listed in the legend. The best-fit parameters of our model are listed in Tab. 3.

peratures $T_{\text{med},V}^{(i)}$, angles of rotation α_i , standard deviations along the two principal axes $\sigma_{1,i}$, $\sigma_{2,i}$, and the volume fraction $f_V^{(i)}$. Note that the combined volume fraction from all phases combined is unity by definition.

We can obtain the marginalized PDFs by integrating the 2D PDFs along one of the axes. For example, 1D volume-PDF of temperature in log space is,

$$\mathcal{P}_V(y) = \sum_i \frac{f_V^{(i)}}{2\sigma_{1,i}\sigma_{2,i}\sqrt{\pi A_i}} \exp\left\{-\frac{(y - y_i)^2}{4A_i\sigma_{1,i}^2\sigma_{2,i}^2}\right\}, \quad (22)$$

which is again a log-normal PDF centered at y_i with a standard deviation $\sqrt{2A_i}\sigma_{1,i}\sigma_{2,i}$. For the other dimension, i.e., in density, similar log-normal PDF exists centered around x_i with standard deviation $\sqrt{2C_i}\sigma_{1,i}\sigma_{2,i}$.

We can use our three-phase formalism to fit the simulation/observational data and constrain the free parameters for different phases. In the central plot of Fig. 9 in color, we show the volume-weighted 2D histogram of hydrogen number density and temperature of the CGM gas (non-star forming) of one of the halos from the Illustris TNG50-1 cosmological simulation (halo ID-110, snap-84). The selected halo has a virial mass of $1.1 \times 10^{12} h^{-1} M_\odot$ (comparable to the Milky Way halo; Dehnen et al. 2006) and a star-formation rate of $3.63 M_\odot \text{yr}^{-1}$ (similar to the Milky Way SFR of $2.0 \pm 0.7 M_\odot \text{yr}^{-1}$; Elia et al. 2022). The median SFR of COS-Halos galaxies is $\approx 1.06 M_\odot \text{yr}^{-1}$; see Fig. 6 in Werk et al. 2012). The stellar mass of our chosen halo is $6.49 \times 10^{10} h^{-1} M_\odot$ (slightly higher than the Milky Way stellar mass of $6.08 \pm 1.14 \times 10^{10} M_\odot$;

Licquia & Newman 2015) We have approximately fitted the 2D histogram for the Illustris halo with the 2D volume-PDFs of our three-phase model (Eq. 20) by eye. The PDFs for all the expressions in this section use hydrogen number density n_H as it is directly available from the simulation data and is independent of the ionization state. The above choice is convenient since plasma models, which are needed for producing observables, use n_H .

Tab. 3 lists the best-fit parameters and the output parameters of our fitting. We note that the parameters presented here are obtained manually by trial and error and are not quantitative statistical fits. We are working on an automated MCMC (Bayesian) fitting procedure to obtain a robust estimation of the model parameters and their corresponding uncertainties (which can then be propagated to the synthetic observables) by constraining our models with the simulation data. The white rotated ellipses in the central plot are 1σ and 2σ contours of the best fit 2D volume PDFs $\mathcal{P}_V^{2D(i)}(\rho, T)$ for each phase (hot, warm, and cold) from our three-phase model.⁵ The black dotted contours, indicating the 2-D PDF over all phases, show that the three log-normal PDFs capture the core of the three phases. Beyond the core, there is a deviation between the analytic model and the histograms from the simulation. In the future, one may explore going beyond log-normal distributions to include tails. The hot phase is the volume-filling phase, whereas the warm and cold phases occupy a smaller volume. The temperature width of the warm phase is broader compared to the hot and cold phases. The cold phase is almost isothermal at $\sim 10^{4.1}$ K but with a large spread in density. Such broad spread for densities in the cold phase is also inferred from the line emission in the Slug nebula (Cantalupo et al. 2019) and is expected to be a robust feature of all multiphase CGMs. The top and the right panels show the 1D volume PDFs marginalized over temperature and density, respectively. The thick yellow and thin purple solid lines show the simulation data and the corresponding best-fit 1D PDFs, respectively. The dotted colored lines show the contribution from individual phases (hot, warm, and cold) using the best-fit parameters. The marginalized PDFs match the simulation data well.

Similar to the 1D mass-PDF (Eq. 4) discussed in previous sections, we can obtain the 2D mass-PDF in the (x, y) space as

$$\mathcal{P}_M^{2D}(x, y) = \frac{\rho_{\text{med},V}^{(u)}}{\langle \rho \rangle} \sum_i e^x \mathcal{P}_V^{2D(i)}(x, y), \quad (23)$$

which is again log-normal and $\langle \rho \rangle$ is the total average density that can be obtained by the normalization condition as (integrating above over x and y),

$$\frac{\langle \rho \rangle}{\rho_{\text{med},V}^{(u)}} = \sum_i f_V^{(i)} \exp\left\{x_i + \sigma_{1,i}^2 \sigma_{2,i}^2 C_i\right\}.$$

The mass fraction $f_M^{(i)}$ of each phase is then given by

$$f_M^{(i)} = \frac{f_V^{(i)} \exp\left\{x_i + \sigma_{1,i}^2 \sigma_{2,i}^2 C_i\right\}}{\sum_i f_V^{(i)} \exp\left\{x_i + \sigma_{1,i}^2 \sigma_{2,i}^2 C_i\right\}}. \quad (24)$$

Unlike volume fraction $f_V^{(i)}$ which is a model parameter, mass fraction $f_M^{(i)}$ is a derived quantity and depends on other free parameters.

⁵ Unlike a 1-D Normal distribution for which 34% and 95% of random deviates lie within 1σ and 2σ , respectively, the corresponding numbers in 2-D are 39% and 86%.

Marginalization of the mass PDF gives⁶

$$\mathcal{P}_M(y) = \sum_i \frac{f_M^{(i)}}{2\sigma_{1,i}\sigma_{2,i}\sqrt{\pi A_i}} \exp\left\{-\frac{(y - y_i + B_i\sigma_{1,i}^2\sigma_{2,i}^2)^2}{4A_i\sigma_{1,i}^2\sigma_{2,i}^2}\right\}, \quad (26)$$

which is again a log-normal PDF.

The 2D histogram in the central panel of Fig. 9 shows that the hot phase is volume-filling and has a lower density in contrast to the cold phase, which is dense but occupies a minuscule fraction of the total volume. The luminosity of the gas at temperature T is $L \propto n^2\Lambda[T]V$. Just like mass, it is important to know the luminosity contributed at different temperatures, especially when CGM emission mapping is expected to be common in the near future (e.g., Tuttle et al. 2019). We obtain the 2-D luminosity PDF,

$$\mathcal{P}_L^{2D}(x, y) = \frac{(\rho_{\text{med},V}^{(u)})^2}{\langle L \rangle} \sum_i e^{2x} \Lambda(y) \mathcal{P}_V^{2D(i)}(x, y), \quad (27)$$

where $\langle L \rangle$ is the volume-averaged luminosity that can be obtained from the normalization condition $\int \mathcal{P}_L^{2D}(x, y) dx dy = 1$.

For the results in this section, we assume the CGM metallicity to be temperature (phase) independent and fixed to a constant value of $0.3 Z_\odot$. Further, we assume that the cooling function only depends on temperature (general case can be treated numerically; see Appendix C for details). This assumption is strictly valid in collisional ionization equilibrium (CIE). However, we adopt a temperature-dependent cooling function for plasma in photo+collisional-ionization equilibrium (PIE) in presence of Haardt-Madau extragalactic UV radiation (Haardt & Madau 2012) at a redshift of 0.2. Our cooling function was generated using CLOUDY for a plasma having hydrogen number density fixed to $2.0 \times 10^{-5} \text{ cm}^{-3}$ (the average hydrogen density obtained by numerically integrating over our analytic volume PDF; Eq. 20). This simplifying assumption allows us to obtain an analytic form for the 1-D luminosity PDF marginalized over density (using Eq. 25 with $p = 2$ and following the same procedure as for the mass PDF). The marginalized luminosity PDF is

$$\mathcal{P}_L(y) = \sum_i \frac{f_L^{(i)} \Lambda(y, Z/Z_\odot)}{2\sigma_{1,i}\sigma_{2,i}\sqrt{\pi A_i}} \exp\left\{-\frac{(y - y_i + 2B_i\sigma_{1,i}^2\sigma_{2,i}^2)^2}{4A_i\sigma_{1,i}^2\sigma_{2,i}^2}\right\}, \quad (28)$$

where

$$f_L^{(i)} = \frac{(\rho_{\text{med},V}^{(u)})^2}{\langle L \rangle} f_V^{(i)} \exp(2x_i + 4\sigma_{1,i}^2\sigma_{2,i}^2 C_i)$$

is the luminosity fraction of phase i , and Z/Z_\odot is the gas metallicity with respect to solar. Note that the luminosity PDF departs from log-normal because of the cooling function.

Fig. 10 shows the 1D PDFs in temperature. The solid lines

Table 3. Parameters of the three-phase CGM model*

Input Parameters	Value
$f_V^{(h)}, f_V^{(w)}, f_V^{(c)}$ [percent]	97.8, 2.04, 0.16
$T_{\text{med},V}^{(u)}, T_{\text{med},V}^{(h)}, T_{\text{med},V}^{(w)}, T_{\text{med},V}^{(c)}$ [log ₁₀ K]	5.0, 5.79, 4.90, 4.10
$n_{H,\text{med},V}^{(u)}, n_{H,\text{med},V}^{(h)}, n_{H,\text{med},V}^{(w)}, n_{H,\text{med},V}^{(c)}$ [log ₁₀ cm ⁻³]	-5.00, -4.85, -4.10, -2.96
$(\sigma_1^{(h)}, \sigma_2^{(h)}), (\sigma_1^{(w)}, \sigma_2^{(w)}), (\sigma_1^{(c)}, \sigma_2^{(c)})$	(0.63, 0.40), (0.56, 1.20), (1.10, 0.15)
$\alpha^{(h)}, \alpha^{(w)}, \alpha^{(c)}$ [deg]	19, 55, 176
Z/Z_\odot	0.3
Output Parameters	Value
$f_L^{(h)}, f_L^{(w)}, f_L^{(c)}$ [percent]	29.97, 25.25, 44.69
$f_M^{(h)}, f_M^{(w)}, f_M^{(c)}$ [percent]	73.32, 12.03, 11.90
$M_{\text{CGM}} [h^{-1} M_\odot]$ (gas mass)	9.92×10^{10}
$\langle n_H \rangle [\text{cm}^{-3}]$	2.2×10^{-5}

* This TNG50-1 halo at $z = 0.2$ has a halo mass $M_{200} = 1.10 \times 10^{12} h^{-1} M_\odot$, stellar mass $M_* = 6.46 \times 10^{10} h^{-1} M_\odot$, star formation rate $\dot{M}_{\text{SFR}} = 3.63 M_\odot \text{ yr}^{-1}$ & virial radius $r_{200} = 188.5 h^{-1} \text{ kpc} = 333.1 \text{ kpc}$.

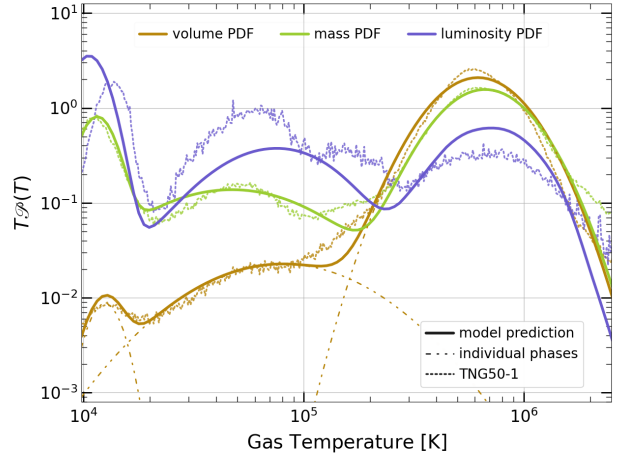


Figure 10. The 1D volume PDFs in temperature marginalized over density. The dashed lines are PDFs from the Illustris TNG50-1 halo (halo ID-110, snap-84). The solid lines show three-phase model PDFs (Eqs. 22, 26 and 28) with best-fit parameters listed in Tab. 3. Note that the three-component Gaussian model captures the qualitative trends correctly. The hot, warm, and cold volume PDFs peak at $\sim (10^{5.8}, 10^{5.2}, 10^{4.1})$ K respectively.

are from our best-fit model with the 2D PDFs in volume mass and luminosity marginalized in density (Eqs. 22, 26 and 28). The dashed lines are 1D temperature PDFs from Illustris TNG50-1 data weighted by volume, mass, and luminosity of the simulation cells.⁷ Our three-phase model is able to capture the hot, warm, and cold phases for all three PDFs. The hot phase dominates the volume (and to a lesser extent mass), whereas luminosity has a dominant contribution from the cold and intermediate phases.

3.1 Synthetic observables from three phase model

We now move on to generate synthetic observables for our three-phase model. We extend the method to obtain observables with

⁶ A useful identity is

$$\int e^{px} \mathcal{P}_V^{2D(i)}(x, y) dx = \frac{f_V^{(i)}}{2\sigma_{1,i}\sigma_{2,i}\sqrt{\pi A_i}} \times \exp\left\{-\frac{[y - y_i + pB_i\sigma_{1,i}^2\sigma_{2,i}^2]^2}{4A_i\sigma_{1,i}^2\sigma_{2,i}^2} + p^2 C_i \sigma_{1,i}^2 \sigma_{2,i}^2 + p x_i\right\}. \quad (25)$$

⁷ The luminosity PDF of the warm phase is underestimated by our model, possibly due to the simple modeling of radiative cooling using a temperature-dependent cooling function with $Z = 0.3Z_\odot$.

1D PDFs in earlier sections to using 2D PDFs. For example, the expression for the column density of a particular ion (say OVI) remains unaltered from Eqs. 16 and 17, but $I^{(i)}$ is now expressed as

$$I^{(i)} = \int d\rho dT \left(\frac{\rho}{\mu_H^{(i)} m_p} \right) \mathcal{P}_V^{2D(i)}(\rho, T) f_{\text{OVI}}(\rho, T). \quad (29)$$

Similarly, we can obtain the expressions for EM, DM, and other observables which now include 2D integrals.

Fig. 11 shows the column density of MgII (cold $\sim 10^4$ K phase tracer) and OVI (warm phase $\sim 10^{5.5}$ K tracer) ions using solid, dotted and dashed lines for different variants of our three-phase model. We use our fast plasma modeling code *AstroPlasma* to evaluate the ion fractions at each ρ, T appearing in the integrals of the form presented in Eq. 29 and obtain the (volume-weighted) average ion density. The plasma is assumed to be in photo+collisional ionization equilibrium (PIE) at a redshift of 0.2 in the presence of Haardt-Madau extragalactic UV background (Haardt & Madau 2012). We use the average ion density for this one-zone model to evaluate the column density profiles shown by the solid lines. Moving beyond the one-zone model, this average density is then used as the normalization factor n_0 appearing in Eq. B3 to obtain the column density for power-law profiles of number density in the CGM. The column densities of OVI and MgII for these power-law density profiles are shown using the dotted and dashed lines in Fig 11.⁸ Circles (detections), upper triangles (lower limits), and lower triangles (upper limits) indicate the observed column densities from different surveys. To mitigate bias, we plan to include observations from more surveys in the future, like the COS-Weak (Muzahid et al. 2018) and the MAGG surveys (Dutta et al. 2020), for which the virial radii of the foreground absorbing galaxies are not readily available and needs to independently determined from galaxy surveys, for example, by using halo abundance matching (Churchill et al. 2013).

While our MgII column density profiles pass through the data points, the OVI columns are somewhat underestimated. This is also reflected in a lower X-ray surface brightness estimate (see Tab. 4). This is due to a lower hot/warm phase (median) density and temperature in our chosen TNG50-1 halo than the Milky Way estimates. This, however, is not too surprising since cosmological simulations show a large scatter in CGM properties at a given mass (Ramesh et al. 2023) due to feedback, mergers, and different evolution histories of different halos. Detailed analysis of such variations and their implication on our models and synthetic observables is left for future. Also note that the large variation in MgII columns as compared to OVI in observed data is a signature of the patchiness of cold clouds, making them frequent only along a few sightlines as compared to a more area-filling warm phase (see discussion in section 4.2). These CGM models, therefore, provide a baseline estimate and need to be complemented with a model of discrete clouds to achieve better match with different multi-wavelength observations.

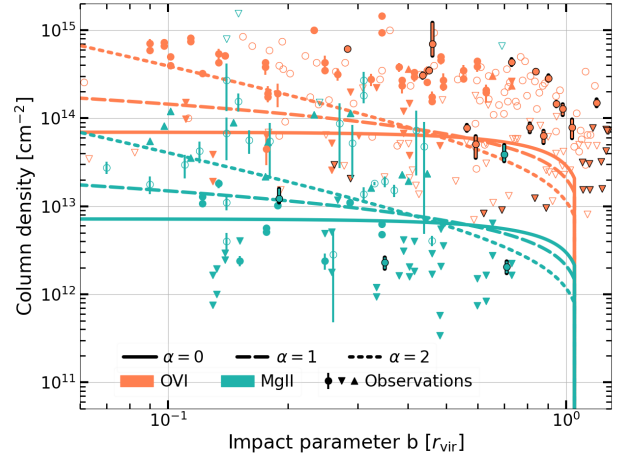


Figure 11. Column densities of OVI and MgII ions as a function of impact parameter predicted by our best-fit three-phase model. Observed columns from different surveys are shown with circles (detections), upper triangles (lower limits), and lower triangles (upper limits). Observations from different surveys that are shown here are from the COS-Halos survey (Tab. 3 from Werk et al. 2013) in cyan/orange filled markers, CGM² survey (Tab. 3 from Tchernyshyov et al. 2022) in open orange markers, MAGnCAT survey (Tab. 1 from Nielsen et al. 2016) in open cyan markers, and CUBS survey (Tab. A1 & Tab. 1 from Qu et al. 2023 for MgII and Tab. B1 from Qu et al. 2024 for OVI) in filled cyan/orange markers with black borders. The galaxies from the COS-Halos and the MAGnCAT surveys have mass and size comparable to the Milky Way (c.f. Tab. 2 from Tumlinson et al. 2013 for COS-Halos & Tab. 1 from Nielsen et al. 2016 for MAGnCAT). The one-zone assumption (solid lines) can be relaxed by assuming a power-law profile with index α (Eq. B1; see Appendix B for details), keeping the total gas mass in the CGM constant (shown by the dashed [$\alpha = 1$] and dotted [$\alpha = 2$] lines). The column density of the OVI is better modeled with a steeper profile ($\alpha = 2$).

4 DISCUSSION

Two approaches to model the CGM are used commonly: (i) 1D profiles (hydrostatic or purely phenomenological) of the dominant hot phase and (ii) numerical simulations of the multiphase CGM that incorporate gas at all temperatures $\gtrsim 10^4$ K. While approach (i) may be satisfactory for the hot phase and can be confronted with X-ray observations, it does not incorporate warm and cooler phases routinely observed in quasar absorption line surveys of the CGM. Approach (ii), while simulating gas with a range of temperatures, also suffers from drawbacks such as computational expense, insufficient resolution to resolve the structure of cooler phases, dependence on subgrid physics, and a limited statistical sample.

In this context, we present a flexible analytic framework for modeling multiphase gas with log-normal distributions that are not only analytically tractable but also motivated by numerical simulations. Our approach can incorporate inputs constrained by numerical simulations and can quickly produce synthetic observables that can be tested against multi-wavelength observations. We can study not just trends with halo mass and environment, but this formalism also provides a baseline prediction for tracers of cold/warm gas, which can be made more realistic by incorporating clouds with non-trivial area covering fraction discussed later in this section 4.2.

⁸ We can relax the assumption of a constant density in the one-zone CGM model by assuming a power-law radial density profile with index α (Eq. B1). The normalization is chosen to maintain the same CGM mass (see Appendix B for details). Instead of self-consistently re-calculating the ionization in power-law profiles, which is computationally expensive, we simply rescaled the ion densities from the one-zone model.

4.1 Interpreting X-ray observations

Interpretation of X-ray emission spectra involves breaking up the observed spectrum into emission from different sources such as the CGM, the local hot bubble (Liu et al. 2016), cosmic X-ray background (Gilli et al. 2007), and solar wind charge exchange (Ponti et al. 2023b).

In addition to these sources, many recent observations of X-ray emission from the Milky Way CGM (Das et al. 2019b; Bluem et al. 2022; Ponti et al. 2023b) consider two isothermal components (APEC models; Smith et al. 2001). The dominant contribution among these two components comes from the gas at the virial temperature of the Galaxy (~ 0.2 keV) while the sub-dominant (about an order of magnitude lower in emission) contribution is from an additional phase at a higher temperature ~ 0.7 keV. In some of these works, the physical origin of this ~ 0.7 keV gas is the Galactic coronal disk maintained by supernovae-driven outflows (e.g., Bregman 1980). However, the emission from the physical disk contributes not only to the ~ 0.7 keV APEC component in the X-ray emission but also to the ~ 0.2 keV component at virial temperature (Kaaret et al. 2019). Some observations attribute the physical origin of the X-ray emission from the entire ~ 0.2 keV component (~ 0.2 keV isotherm in the APEC model) to the CGM (Ponti et al. 2023b) but it might have a non-negligible contribution from the disk.

Spectral fitting of APEC models along any single sightline cannot distinguish among physically distinct multiple components with the same temperature contributing to the total emission. Considering the EM from only the CGM of the Milky Way, towards and away from the Galactic center, one expects a variation of $\lesssim 2$ for high Galactic latitudes ($|b| \gtrsim 30^\circ$; see middle column of Fig. 6). However, the variation as observed by Bluem et al. 2022 at the same latitudes is $\gtrsim 3$, which favors models that include a coronal disk component (see also Ponti et al. 2023b). The presence of such a disk has also been pointed out in previous works (Yamasaki & Totani 2020; Kaaret et al. 2019). Therefore, we highlight the possibility that the ~ 0.2 keV isothermal APEC model termed as the CGM in some observations might actually be *disk+CGM* and all the gas at the virial temperature cannot be assigned to just the spherical halo of the Milky Way. X-ray surveys such as the eROSITA all-sky survey (eRASS; Predehl et al. 2021) are expected to map out the diffuse X-ray emission at a range of latitudes and longitudes and help us break the degeneracy between various physical components that produce the X-ray spectra along different directions. Our models assume smooth disk and CGM, but the true gas distribution can have large variations (e.g., Das et al. 2021a), which will affect our predictions quantitatively. Moreover, a careful statistical estimate of parameters of even our smooth model is left for future.

4.2 Finite-size clouds & observational implications

In this paper, all the LOS integrals were computed in the mist limit (Fig. 2b) where a small volume fraction is filled by the cold/warm phases, comprising an infinite number of clouds each of which is infinitesimally small. However, real CGM clouds have a finite size, and the observed area filling fraction is smaller than unity (and different for different ions and column density thresholds of detection) for the tracers of warm/cold phase (Augustin et al. 2021). Thus, clouds do not cover all the sightlines, and this natural variability needs to be considered when predicting the column densities of ions. A comprehensive analysis of cloud morphology and their distribution is beyond the scope of the present paper. Nevertheless, in this subsection, we discuss the ‘mist’ limit of cold/warm clouds

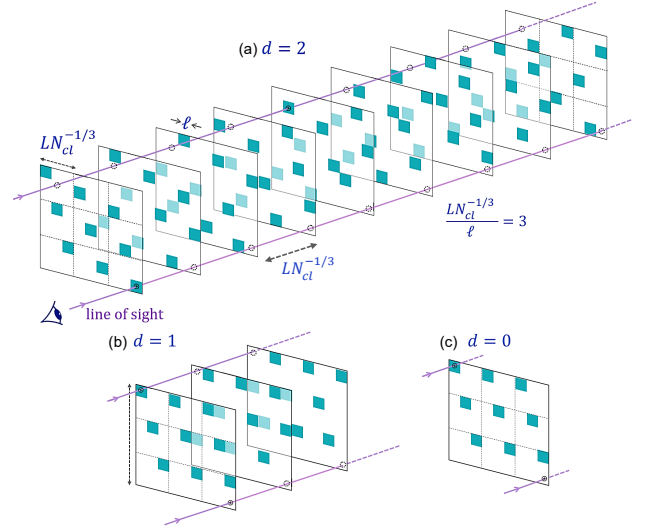


Figure 12. A portion of the CGM with clouds (a) spread out in two directions perpendicular to the LOS ($d = 2$), (b) spread out in one direction perpendicular to LOS ($d = 1$), and (c) no spread perpendicular to LOS ($d = 0$). Each blue square represents cubical clouds of size l . Each 3×3 layer shows the arrangement of cubes of side $LN_{\text{cl}}^{-1/3}$ (mean distance between clouds for the maximally separated, most probable arrangement), each of which contains just one cloud. In all cases shown (a), (b), and (c), every sightline covered by a cloud will have overlapping clouds if the pattern is repeated along the LOS. There are $f_V^{-d/3}$ number of clouds spread maximally in d dimensions perpendicular to LOS (see section 4.2). The number of clouds aligned along LOS with non-zero column is thus $N_{\text{cl}}^{1/3} / f_V^{-d/3}$ and the column density is $N = nl \times N_{\text{cl}}^{1/3} / f_V^{-d/3} = nL f_V^{(1+d)/3}$. From the $d = 2$ (the mist limit) to $d = 0$, the observed column would be enhanced by a factor of $f_V^{-2/3}$ (~ 100 for our fiducial values!).

in the CGM and demonstrate how such a configuration provides the most probable baseline configuration for the column density of ions. Additionally, we discuss some qualitative effects of a more realistic spatial distribution of clouds (departing from the mist limit) on the observables, which can potentially lower as well as increase the observed column densities of different ions, resulting in large scatter. Cloud distribution also affects the observed area covering fractions of the absorbing clouds.

The column densities and covering fractions of the clouds (corresponding to the phases with small volume filling fractions) depend on their arrangement within the CGM volume. For simplicity, let us consider N_{cl} non-overlapping clouds, each assumed to be a cube of side l with gas density n , arranged within a cube of side L (representing the CGM) such that $l \ll L$. The volume fraction of clouds f_V is given by $f_V = (l/L)^3 N_{\text{cl}}$. We can express the cloud length l in terms of f_V and N_{cl} as $l = L f_V^{1/3} N_{\text{cl}}^{-1/3}$. The number of MgII clouds identified in Illustris TNG50-1 halos is $N_{\text{cl}} \gtrsim 10^4$ (Nelson et al. 2020; Dutta et al. 2022). We adopt a fiducial value of $N_{\text{cl}} = 10^6$ to account for clouds smaller than the resolution limit of typical state-of-the-art cosmological simulations. The fiducial volume fraction of the cold phase is taken as $f_V = 10^{-3}$, consistent with our Illustris TNG50-1 halo (see $f_V^{(c)}$ in Tab. 3); these give $l/L = 0.001$ or $l = 100$ pc for a CGM size of 100 kpc.

The maximum possible column density N_{max} is for the highly improbable arrangement of independent clouds when all clouds lie along the line of sight and the value, in this case, is $N_{\text{max}} = nL N_{\text{cl}} = nL f_V^{1/3} N_{\text{cl}}^{2/3} (= 1000nL$ for fiducial parameters; n is the local num-

ber density of the ion of interest within the cloud).⁹ As the projected plane is covered by just one cloud, the area covering fraction for such a high column density is $f_A = l^2/L^2 = f_V^{2/3} N_{\text{cl}}^{-2/3}$ (only 10^{-6} for fiducial parameters!). The number of clouds along this LOS is $N_{\text{cl,LOS}} = N_{\text{cl}}$ while any other parallel sightline encounters no cloud. The product of the column density and the area covering fraction is $N f_A = n L f_V$, which is fixed for all cloud arrangements because $n f_V L^3 = N f_A L^2$ is just the total number of ions in the CGM, which is assumed to be a constant. The configuration where all clouds are lined up next to each other is however extremely unlikely.

Fig. 12 shows specific examples of different arrangements of clouds. Panel (a) shows the *most probable separation of clouds* that corresponds to an equal separation between them; i.e., the mean distance between clouds is $(L^3/N_{\text{cl}})^{1/3} = L N_{\text{cl}}^{-1/3}$. This is because the volume of the CGM available for each non-overlapping cloud is L^3/N_{cl} . In one of the most likely arrangements shown in (a) clouds are maximally spread out in all directions (along the LOS and also along both directions perpendicular to it). As an example, we choose the mean separation between the clouds to be three cloud sizes (i.e., $L N_{\text{cl}}^{-1/3}/l = 3$). Since there are $N_{\text{cl}}^{1/3}$ clouds in a direction, and they are maximally separated in the perpendicular plane ($d = 2$), the number of clouds overlapping along the LOS is $N_{\text{cl,LOS}} = N_{\text{cl}}^{1/3}/(L N_{\text{cl}}^{-1/3}/l)^2 = f_V^{2/3} N_{\text{cl}}^{1/3}$. The column density is, therefore, $N = (nl) N_{\text{cl,LOS}} = n L f_V$. Note that this is nothing but the integral of global number density along the LOS (see Eqs. 14 & 16), which corresponds to the column density in the mist limit. *Thus, the integral of global number density along the LOS corresponds to the most probable arrangement of independent tiny clouds with minimal overlap along the way and can be taken as the baseline value for comparing with observations.* Since every sightline (both along and perpendicular to the LOS) has equal column density in this case, the area covering fraction is 1 (assuming $N_{\text{cl}} > f_V^{-2}$ so that all sightlines intercept at least one cloud on average). In this case, on moving the LOS in any direction by one cloud size, the encountered cloud configuration is statistically identical.

If clouds are spread out only in one direction in the plane perpendicular to the LOS ($d = 1$; see Fig. 12(b)), the column density is $N = n L f_V^{2/3}$ and the number of clouds along the LOS is $N_{\text{cl,LOS}} = N_{\text{cl}}^{1/3}/(L N_{\text{cl}}^{-1/3}/l) = f_V^{1/3} N_{\text{cl}}^{1/3}$, with area covering fraction $f_A = l N_{\text{cl}}^{1/3}/L = f_V^{1/3}$. In all cases, the product of the area covering fraction and the column density is a constant equal to $n L f_V$, as explained in the previous paragraphs. The clouds overlap in all dimensions across the LOS in Fig. 12(c) corresponding to $d = 0$ and the column density is $n L f_V^{1/3}$, such that every sightline with non-zero column has $N_{\text{cl}}^{1/3}$ clouds. Therefore, in general, for any configuration with spread in d number of directions ($d = 0/1/2$), the total number of clouds along the LOS is $N_{\text{cl,LOS}} = N_{\text{cl}}^{1/3}/(L N_{\text{cl}}^{-1/3}/l)^d = N_{\text{cl}}^{1/3} f_V^{d/3}$, which gives the column density $N = N_{\text{cl,LOS}} \times nl = n L f_V^{(1+d)/3}$.

A smaller area covering fraction implies that the value of column density along some sightlines that encounter warm/cold clouds can be much larger than our mist estimate. Similarly, some other sightlines would encounter a significantly lower column. This deviation from the mist estimate is expected to be larger for phases with smaller volume fraction f_V , such as MgII tracing 10^4 K clouds (see

Fig. 10; Tab. 3). A large fluctuation in MgII columns (in comparison to OVI which traces a warmer phase) and a small covering fraction implied by data in Fig. 11 can be explained by variable overlap of clouds along various sightlines. The column density can, therefore, be either enhanced or diminished by orders of magnitude compared to our mist estimate. Observations provide a statistical sample of several LOS and contain upper limits that lie below the mist prediction which can be interpreted with the baseline predictions of the mist limit; these sightlines simply do not encounter substantial cold clouds!

The UV absorption spectra indicate the presence of several components along the LOS (e.g., Stocke et al. 2013; Werk et al. 2014; Zahedy et al. 2019; Haislmaier et al. 2021), indicating multiple clouds along a typical LOS. In the case of lensing of the background quasar, an estimate of the transverse extent of clouds (e.g., Rudie et al. 2019; Augustin et al. 2021) can provide crucial information on cloud properties. Observational constraints such as these, combined with extensions of the toy cloud model presented here, can provide a wealth of information about the properties of the CGM clouds in different phases despite being unresolved.

4.3 Future directions

In this paper, we have only focused on the emission and dispersion measures and column densities, but observations provide a wealth of other diagnostics including kinematic information. Our models can be extended to include velocity distributions, which may be drawn from PDFs with 1-point and 2-point statistics consistent with observations and galaxy formation simulations. In the following, we briefly explain the utility of a library of different CGM models that can be compared with independent observational constraints.

4.3.1 Towards a library of models

In this paper, we introduced probabilistic models of the CGM, including a new three-phase model. We used these models to predict various observables and compared them with observations. A combination of various observational constraints helps us quantitatively assess various models (see Tab. 4). This motivates an effort towards developing a library of models that can be continuously expanded to include the existing and new CGM models of varying complexity, from simple 1D profiles to 2D axisymmetric rotating models (e.g., Sormani et al. 2018), and to models like ours based on PDFs. In addition to CGM observables highlighted in this paper, we aim to add more observables such as the scattering measure (e.g., Ocker et al. 2021) which is sensitive to the size of CGM clouds, and thermal Sunyaev-Zeldovich y -parameter (e.g., Bregman et al. 2022) which is an excellent tracer of the CGM mass. We can also include models of magnetic fields and turbulence in the CGM. These models can constrain the turbulent and magnetic support in the CGM when compared against the Faraday rotation measures observed from the CGM of external galaxies (Hafen et al. 2024; Böckmann et al. 2023).

Such a library of models and observable predictions would enable one to quickly infer the physical properties and chemical composition of the CGM from observations, constrain model parameters, break degeneracy across models, and rank models according to the number of independent observations that they can match. We aim to expand our public code repository `MultiphaseGalacticHaloModel` (link provided in the Data availability section 7) into a large library of CGM models and observables.

⁹ Note that the combined length of the cloud, in this case, is $l N_{\text{cl}} = L f_V^{1/3} N_{\text{cl}}^{2/3} \gg L$. We consider this highly improbable case only for illustration of an extreme limit.

Table 4. Comparison of models with observations *

Observables	Observed value	Models				
		$\gamma = 1^{**}$	$\gamma = 5/3^{**}$	three-phase CGM		
				$\alpha = 0$	$\alpha = 1^{***}$	$\alpha = 2$
Dispersion measure (l,b) [pc cm ⁻³] CHIME [Bhardwaj +21 [§]]	(142°, 41°) [30]	30.11 (7.04)	20.55 (7.04)	13.20 (7.04)	21.81 (7.04)	75.37 (7.04)
Emission measure (l,b) [10 ⁻² pc cm ⁻⁶] eFEDS [Ponti +23 [†]]	(230°, 30°) [2.9 – 3.1]	1.33 (0.77)	0.99 (0.77)	0.79 (0.77)	0.98 (0.77)	18.45 (0.77)
Surface brightness [10 ⁻¹³ erg cm ⁻² s ⁻¹ deg ⁻²] eFEDS [Ponti +23 [‡]]	(230°, 30°) 0.3-0.6 keV: [15.6] 0.6-2.0 keV: [4.9]	14.22 (11.04) 1.78 (1.42)	13.66 (11.04) 1.84 (1.42)	11.15 (11.04) 1.44 (1.42)	11.17 (11.04) 1.45 (1.42)	14.72 (11.04) 1.55 (1.42)
Ion columns (cm ⁻²)						
O VIII	2.4 × 10 ¹⁵ – 4.2 × 10 ¹⁵	2.6 × 10 ¹⁴ – 1.1 × 10 ¹⁶	7.6 × 10 ¹³ – 7.7 × 10 ¹⁵	5.3 × 10 ¹⁴ – 1.8 × 10 ¹⁵	3.6 × 10 ¹⁴ – 4.7 × 10 ¹⁵	1.9 × 10 ¹⁴ – 2.4 × 10 ¹⁶
O VII	3.6 × 10 ¹⁵ – 9.6 × 10 ¹⁵	3.5 × 10 ¹⁴ – 3.3 × 10 ¹⁶	8.9 × 10 ¹³ – 1.7 × 10 ¹⁶	9.6 × 10 ¹⁴ – 3.2 × 10 ¹⁵	6.6 × 10 ¹⁴ – 8.6 × 10 ¹⁵	3.6 × 10 ¹⁴ – 4.4 × 10 ¹⁶
O VI	4.5 × 10 ¹³ – 1.4 × 10 ¹⁵	1.1 × 10 ¹³ – 1.7 × 10 ¹⁵	4.6 × 10 ¹² – 8.7 × 10 ¹⁴	4.2 × 10 ¹³ – 1.4 × 10 ¹⁴	2.8 × 10 ¹³ – 3.7 × 10 ¹⁴	1.5 × 10 ¹³ – 1.9 × 10 ¹⁵
NV	4.9 × 10 ¹³ – 1.5 × 10 ¹⁴	5.4 × 10 ¹¹ – 1.5 × 10 ¹⁴	1.2 × 10 ¹¹ – 6.2 × 10 ¹³	4.1 × 10 ¹² – 1.4 × 10 ¹³	2.8 × 10 ¹² – 3.7 × 10 ¹³	1.5 × 10 ¹² – 1.9 × 10 ¹⁴
Mg II	2.4 × 10 ¹² – 1.8 × 10 ¹³	4.1 × 10 ⁹ – 1.8 × 10 ⁹	2.4 × 10 ³ – 4.3 × 10 ⁸	5.7 × 10 ¹² – 1.9 × 10 ¹³	3.9 × 10 ¹² – 5.1 × 10 ¹³	2.1 × 10 ¹² – 2.6 × 10 ¹⁴

Note that for ion columns, only detections are listed in the second column "Observed value". In case of just detections, only upper or lower limits exist and no specific observed values are available (*triangles* in Fig. 5). For NV there mostly exists upper limits in detection. *Values in parentheses show the disk contribution, when considered.*

* Colors indicate agreement with corresponding observation [Green: Good; Yellow: Moderate; Red: Unacceptable].

** For these, we consider isochoric modification.

*** $\alpha = 1$ is a singularity in Eq. B3), so we used $\alpha = 1.01$.

§ Tab. 2 in Bhardwaj et al. 2021

† Tab. 2 in Ponti et al. 2023b

‡ Tab. 4 in Ponti et al. 2023b

We discuss the CGM model proposed in Yamasaki & Totani 2020 as an example to demonstrate the insights that can be gained by comparing models to multi-wavelength observations. In this work, the disk emission at the virial temperature of the spherical CGM is approximately an order of magnitude higher than the emission from the CGM gas along any line of sight (e.g., see their Fig. 1). However, the disk contribution in our models is either slightly higher or comparable to the spherical CGM (see Fig. 8). Considering only Milky Way observations, it is not possible to break the degeneracy between our models and the Yamasaki & Totani 2020 model. Low disk contribution to EM in the Yamasaki & Totani 2020 model is a result of a low CGM central density of, $3.7 \times 10^{-4} \text{ cm}^{-3}$ in contrast to our models ($\gamma = 1, 5/3$ unmodified profiles) with the CGM density at 10 kpc $\sim 10^{-3} \text{ cm}^{-3}$ (see Fig. 4). In the observations of external CGMs, for most sightlines the contribution of the central disk is negligible, and the density of the CGM in the Yamasaki & Totani 2020 model is too low to produce a sufficiently large column of ions like OVI, NV. We can, therefore, justify the choice of parameters favoring a higher density CGM as used in our models by considering UV absorption studies of the CGM of Milky Way-like external galaxies. We also have to bear in mind that the CGM for the same halo mass can show a large scatter in physical properties (Ramesh et al. 2023).

4.3.2 Fast plasma modeling repository: AstroPlasma

Generating observables like dispersion/emission measures or column densities of ions from fluid fields like density and temperature requires plasma modeling. One of the goals of our code base is to be computationally efficient for quick exploration of the parameter space of various CGM models and to compare with different observations. AstroPlasma is a public code repository written as a standalone package that can provide functions that generate ioniza-

tion properties (e.g., various ion fractions, mean molecular weight) for conditions in the CGM.

AstroPlasma uses a large database of pre-run CLOUDY (Ferland et al. 2017) models to interpolate the ionization properties for a range of CGM plasma conditions. This database can be expanded or updated as needed. We are able to achieve a low computational cost for evaluating observables by eliminating the need for on-the-fly calculation of expensive chemical networks. AstroPlasma instead looks up its database of CLOUDY models to interpolate the plasma properties across densities, temperatures, and metallicities. Currently, our database has plasma conditions for collisional ionization equilibrium (CIE) and photo-ionization equilibrium (PIE) in the presence of Haardt-Madau UV background (Haardt & Madau 2012) at different cosmological redshifts. We assume optically thin conditions and do not consider any radiative transfer effects. Appendix A illustrates some common usage of AstroPlasma.

4.4 Comparison with related works

Single phase models (e.g., Maller & Bullock 2004; Sharma et al. 2012b; Miller & Bregman 2013; Nakashima et al. 2018; Voit 2019) typically used to model the hot phase are insufficient even qualitatively to reproduce the properties of the observed multiphase CGM. FSM17 made an advance towards modeling the warm phase traced by OVI by adding a phase at $10^{5.5} \text{ K}$ with a log-normal volume distribution over temperature on top of the isothermal hot phase. Later, Faerman et al. (2020) reproduced OVI column densities by assuming an isentropic, hydrostatic hot gas profile (with significant non-thermal pressure support) for which the outer temperatures are small enough to reproduce OVI column densities. Since this model cannot produce cold gas, Faerman & Werk (2023) recently extended their isentropic model with non-thermal pressure support (due to turbulence, cosmic rays, and magnetic fields) to include a cold component at $\sim 10^4 \text{ K}$ in photo-ionization and thermal equilibrium. The

cold phase with a small volume fraction ($f_V^{(c)} \sim 0.01$) and a non-thermal pressure fraction higher than the hot phase could reproduce the ballpark values of the column densities of the ions tracing the cold phase. Because of the lack of $\sim 10^5$ K gas in this model, it generally under-predicts the columns of intermediate ions such as CIV and SiIV. Based on PDFs motivated by a large spread in CGM temperatures at most radii in observations and simulations, our approach is fundamentally different and more akin to FSM17.

Ramesh et al. (2023) have systematically analyzed the CGM properties of 132 Milky Way-like halos in Illustris TNG50–1 cosmological galaxy formation simulations. They find a large spread in CGM properties of their sample (e.g., mass fraction in various CGM phases). The CGM properties depend on the specific star formation rate of the galaxy. Similarly, there is a systematic increase in the CGM X-ray luminosity with an increasing stellar mass of the central galaxy. The temperature-density PDF (the colored 2D histograms shown in Fig. 9) of their CGMs is affected by ongoing AGN feedback (see their Fig. 9). Inputs from their statistical study can be incorporated into our formalism, largely motivated by a large spread of densities and temperatures in CGM simulations (see also Esmerian et al. 2021; Fielding et al. 2020, etc.), and variations in CGM properties over a large range of halo masses and redshifts can be quickly calculated.

In between the simple models of hot CGM and complex cosmological simulations lie the high-resolution idealized simulations that focus on the physics of flows and thermodynamics around cold gas moving through the hot CGM (e.g., Armillotta et al. 2016; Gronke & Oh 2018; Kanjilal et al. 2021; Mohapatra et al. 2022, 2023; Yang & Ji 2023). The boundary layers around such clouds are also multiphase with a characteristic volume PDF covering a broad range of temperatures (e.g., see Fig. 5 in Kanjilal et al. 2021, Fig. 4 in Mohapatra et al. 2023) from $\sim 10^4$ K to $\gtrsim 10^6$ K. The relation between density/temperature fluctuations and turbulent Mach number in turbulent cooling layers is fundamentally different from isotropic homogeneous turbulence. For the latter, the rms fluctuations in $\ln \rho / \langle \rho \rangle$ scale as \mathcal{M}^2 (\mathcal{M} is turbulent Mach number) but for radiative turbulence density fluctuations are much higher due to radiative cooling (e.g., Mohapatra & Sharma 2019). The multiphase CGM can be thought of as a superposition of several such clouds, with their radiative boundary layers at intermediate temperatures and the confining pressure decreasing away from the center. Our formalism based on PDFs is also capable of capturing the temperature distribution of such boundary layers. Thus, a description based on PDFs, which is consistent with both the small-scale structure of the CGM clouds and galaxy formation simulations, seems appropriate for studying the CGM as a whole.

5 SUMMARY

Here, we summarize the most important results and implications of our work.

(i) We have highlighted the need to move beyond simple profiles to model the CGM. Simulations, both idealized and cosmological, indicate the cospatial presence of cold, warm, and hot gas. We have shown that a probabilistic model of the multiphase CGM can reliably explain results from multi-wavelength observations (see Figs. 5, 6, 7, 11). These models, despite being more complex, still remain largely analytic. The standout improvement over the existing CGM models like those introduced in Faerman et al. 2017, 2020; Faerman & Werk 2023 is that our probabilistic model can simultaneously explain

the presence of most ions observed in UV absorption spectra of quasar sightlines passing through the CGM of intervening galaxies. Additionally, our probabilistic models match the observations of the Milky Way CGM well. These include dispersion measure from a nearby FRB (Bhardwaj et al. 2021) and X-ray emission measure in the soft X-ray bands (Kaaret et al. 2019; Das et al. 2019a; Bluem et al. 2022; Ponti et al. 2023b).

(ii) We clarify an apparent confusion in the identification of physical sources of diffuse soft X-ray emission spectra from the Milky Way. We highlight that the observed X-ray emission from the gas at the virial temperature of the CGM (~ 0.2 keV) may be dominated by a dense disk rather than the spherically symmetric CGM (see Fig. 8).

The emission from this dense disk in addition to the CGM is degenerate in the isothermal APEC modeling of the X-ray spectrum along a single sightline. This degeneracy can, however, be lifted if the spatial variation of emission measure across multiple sightlines is considered. The disk can contribute to both ~ 0.2 keV phase and the newly introduced phase at ~ 0.7 keV (see Das et al. 2019a; Bluem et al. 2022; Ponti et al. 2023b). Since only the ~ 0.7 keV component is referred to as the Galactic coronal disk in Ponti et al. 2023b, we highlight the possibility that ~ 0.7 keV gas in the disk is but a minor contributor to the X-ray emission, and a significantly larger emission comes from the ~ 0.2 keV phase of the disk. It is also physically plausible to have a dense disk with a broad spread of temperatures between 0.2 keV and 0.7 keV, but this gets decomposed into emission from two components due to the specifics of APEC modeling (e.g., Vijayan & Li 2022). Further investigation on this uncertainty is beyond the scope of this work.

(iii) We address the plausible reason for large variations in the observed cold ion column densities across multiple quasar sightlines through different external galaxies (e.g., see Fig. 11). Starting from the warm to the cold phase, the gas becomes progressively less volume filling. We introduce scaling relations in terms of the number of clouds (N_{cl}) and their volume filling fraction (f_V) that can be qualitatively motivated from the distribution of cold/warm clouds within the CGM (see section 4.2 & Fig. 12). We make baseline predictions of column densities of ions in the mist limit.

(iv) Our work motivates a library of CGM models, and synthetic observables matched against observations (e.g., Tab. 4). Given recent advances across diverse CGM observations across multiple wavelengths, directly comparing a wide range of models to different observations is warranted. When confronted with new observations, a comparative framework can reveal model strengths, weaknesses, and biases. Ultimately, this exercise will help us accurately estimate important physical parameters, such as the fraction of baryons in various phases of the CGM.

A library of models and observables will enable benchmarking against observations and elucidate model limitations and assumptions. We, therefore, create a publicly available code repository called `MultiphaseGalacticHaloModel` and a computationally inexpensive plasma modeling database called `AstroPlasma` to continually encompass existing and future CGM models and compare them with the latest observations.

6 ACKNOWLEDGEMENTS

PS acknowledges a Swarnajayanti Fellowship (DST/SJF/PSA-03/2016-17) and a National Supercomputing Mission (NSM) grant from the Department of Science and Technology, India. Research of AD is supported by the Prime Minister’s Research Fellowship

(PMRF) from the Ministry of Education (MoE), Govt. of India. AD acknowledges Gurkirat Singh for his efforts in building and testing *AstroPlasma*. AD acknowledges Dylan Nelson for his help in processing and analyzing *Illustris* TNG50 data dumps. AD acknowledges Sayak Dutta, Zhijie Qu (屈稚杰), and Sowgat Muza-hid for their help in accessing and analyzing the observational data. AD also acknowledges Yakov Faerman, Gabriele Ponti, Sanskriti Das, Hsiao-Wen Chen (陳曉雯), Andrea Afruni, Priyanka Singh, Kartick Sarkar, Sukanya Mallik, and our anonymous referee for their useful comments and discussions. We thank Gary Ferland and col-laborators for the CLOUDY code. This research also benefited from discussions at *Fundamentals of gaseous halos program (Halo21)*, which was supported in part by grant NSF PHY-2309135 to the Kavli Institute for Theoretical Physics (KITP).

7 DATA AVAILABILITY

We have made all the codes and data used in this paper pub-lic. The CLOUDY-like plasma modeling tool that we developed is hosted in the *GitHub* repo *AstroPlasma*¹⁰ for general use. All the CGM models and the observables used in this work are hosted as a part of an expanding library of CGM models in the *GitHub* repo *MultiphaseGalacticHaloModel*.¹¹ Any other relevant data as-sociated with this article are available to the corresponding author upon reasonable request.

REFERENCES

- Amodeo S., et al., 2021, *Phys. Rev. D*, **103**, 063514
 Armillotta L., Fraternali F., Marinacci F., 2016, *MNRAS*, **462**, 4157
 Asplund M., Grevesse N., Sauval A. J., Scott P., 2009, *ARA&A*, **47**, 481
 Augustin R., Péroux C., Hamanowicz A., Kulkarni V., Rahmani H., Zanella A., 2021, *Monthly Notices of the Royal Astronomical Society*, **505**, 6195
 Bhardwaj M., et al., 2021, *ApJ*, **910**, L18
 Bhattacharyya J., Das S., Gupta A., Mathur S., Krongold Y., 2023, *The Astrophysical Journal*, 952, 41
 Bluem J., et al., 2022, *ApJ*, **936**, 72
 Böckmann K., et al., 2023, *arXiv e-prints*, p. arXiv:2308.11391
 Bregman J. N., 1980, *ApJ*, **236**, 577
 Bregman J. N., Hodges-Kluck E., Qu Z., Pratt C., Li J.-T., Yun Y., 2022, *ApJ*, **928**, 14
 Buie Edward I., Fumagalli M., Scannapieco E., 2020a, *ApJ*, **890**, 33
 Buie Edward I., Gray W. J., Scannapieco E., Safarzadeh M., 2020b, *ApJ*, **896**, 136
 Burchett J. N., et al., 2019, *The Astrophysical Journal Letters*, **877**, L20
 Butsky I. S., et al., 2022, *ApJ*, **935**, 69
 Cantalupo S., et al., 2019, *MNRAS*, **483**, 5188
 Carswell R. F., Webb J. K., 2014, VPFIT: Voigt profile fitting program, Astrophysics Source Code Library (ascl:1408.015)
 Chen H. H.-H., Burkhart B., Goodman A., Collins D. C., 2018, *ApJ*, **859**, 162
 Chen H.-W., et al., 2020, *Monthly Notices of the Royal Astronomical Society*, **497**, 498
 Chen H.-W., et al., 2023, *arXiv e-prints*, p. arXiv:2309.05699
 Choudhury P. P., Sharma P., Quataert E., 2019, *MNRAS*, **488**, 3195
 Churchill C. W., Trujillo-Gomez S., Nielsen N. M., Kacprzak G. G., 2013, *The Astrophysical Journal*, **779**, 87

- Cook A. M., et al., 2023, *arXiv e-prints*, p. arXiv:2301.03502
 Cooper T. J., et al., 2021, *MNRAS*, **508**, 4359
 Crain R. A., McCarthy I. G., Frenk C. S., Theuns T., Schaye J., 2010, *Monthly Notices of the Royal Astronomical Society*, **407**, 1403
 Das S., Mathur S., Nicastro F., Krongold Y., 2019a, *ApJ*, **882**, L23
 Das S., Mathur S., Gupta A., Nicastro F., Krongold Y., 2019b, *The Astro-physical Journal*, **887**, 257
 Das S., Mathur S., Gupta A., 2020, *ApJ*, **897**, 63
 Das S., Mathur S., Gupta A., Nicastro F., Krongold Y., 2021a, *MNRAS*, **500**, 655
 Das S., Mathur S., Gupta A., Krongold Y., 2021b, *ApJ*, **918**, 83
 DeFelippis D., Bouché N. F., Genel S., Bryan G. L., Nelson D., Marinacci F., Hernquist L., 2021, *The Astrophysical Journal*, **923**, 56
 Dehnen W., McLaughlin D. E., Sachania J., 2006, *MNRAS*, **369**, 1688
 Dutta R., et al., 2020, *Monthly Notices of the Royal Astronomical Society*, **499**, 5022
 Dutta A., Sharma P., Nelson D., 2022, *MNRAS*, **510**, 3561
 Elia D., et al., 2022, *ApJ*, **941**, 162
 Esmerian C. J., Kravtsov A. V., Hafen Z., Faucher-Giguère C.-A., Quataert E., Stern J., Kereš D., Wetzel A., 2021, *MNRAS*, **505**, 1841
 Faerman Y., Werk J. K., 2023, *The Astrophysical Journal*, **956**, 92
 Faerman Y., Sternberg A., McKee C. F., 2017, *ApJ*, **835**, 52
 Faerman Y., Sternberg A., McKee C. F., 2020, *ApJ*, **893**, 82
 Fang T., Buote D., Bullock J., Ma R., 2015, *ApJS*, **217**, 21
 Faucher-Giguère C.-A., Oh S. P., 2023, *ARA&A*, **61**, 131
 Faucher-Giguère C.-A., 2020, *Monthly Notices of the Royal Astronomical Society*, **493**, 1614
 Ferland G. J., et al., 2017, *Rev. Mex. Astron. Astrofis.*, **53**, 385
 Fielding D. B., et al., 2020, *ApJ*, **903**, 32
 Fraternali F., 2017, in Fox A., Davé R., eds, *Astrophysics and Space Science Library* Vol. 430, Gas Accretion onto Galaxies. p. 323 (*arXiv:1612.00477*), doi:10.1007/978-3-319-52512-9_14
 Gilli R., Comastri A., Hasinger G., 2007, *A&A*, **463**, 79
 Grand R. J. J., et al., 2019, *Monthly Notices of the Royal Astronomical Society*, **490**, 4786
 Gronke M., Oh S. P., 2018, *MNRAS*, **480**, L111
 Gupta A., Mathur S., Krongold Y., Nicastro F., Galeazzi M., 2012, *ApJ*, **756**, L8
 Gupta A., Mathur S., Galeazzi M., Krongold Y., 2014, *Astrophysics and Space Science*, **352**, 775
 Haardt F., Madau P., 2012, *ApJ*, **746**, 125
 Hafen Z., et al., 2024, *Monthly Notices of the Royal Astronomical Society*, **528**, 39
 Haislmaier K. J., Tripp T. M., Katz N., Prochaska J. X., Burchett J. N., O’Meara J. M., Werk J. K., 2021, *MNRAS*, **502**, 4993
 Henley D. B., Shelton R. L., 2010, *The Astrophysical Journal Supplement Series*, **187**, 388
 Henley D. B., Shelton R. L., 2013, *The Astrophysical Journal*, **773**, 92
 Hirth W., Herbstmeier U., Mebold U., 1992, *Kleinheubacher Berichte*, **35**, 803
 Hummels C. B., et al., 2019, *ApJ*, **882**, 156
 Hummels C. B., Rubin K. H. R., Schneider E. E., Fielding D. B., 2023, *arXiv e-prints*, p. arXiv:2311.05691
 Ji S., et al., 2020, *MNRAS*, **496**, 4221
 Johnson S. D., Chen H.-W., Mulchaey J. S., 2015, *MNRAS*, **449**, 3263
 Kaaret P., et al., 2019, *The Astrophysical Journal*, **884**, 162
 Kaaret P., et al., 2020, *Nature Astronomy*, **4**, 1072
 Kacprzak G. G., Churchill C. W., Murphy M. T., Cooke J., 2015a, *MNRAS*, **446**, 2861
 Kacprzak G. G., Muzahid S., Churchill C. W., Nielsen N. M., Charlton J. C., 2015b, *The Astrophysical Journal*, **815**, 22
 Kanjilal V., Dutta A., Sharma P., 2021, *MNRAS*, **501**, 1143
 Khaire V., Srianand R., 2019, *Monthly Notices of the Royal Astronomical Society*, **484**, 4174
 Kim C.-G., Ostriker E. C., 2018, *The Astrophysical Journal*, **853**, 173
 Körtgen B., Federrath C., Banerjee R., 2017, *MNRAS*, **472**, 2496
 Lehner N., Howk J. C., Wakker B. P., 2015, *ApJ*, **804**, 79
 Lehner N., et al., 2020, *ApJ*, **900**, 9

¹⁰ <https://github.com/dutta-alankar/AstroPlasma>; the code for the accompanying web-server that hosts the *AstroPlasma* database is in a separate *GitHub* repo: <https://github.com/tbhaxor/CloudyInterpolator>.

¹¹ <https://github.com/dutta-alankar/MultiphaseGalacticHaloModel>

- Li Y., et al., 2020, [ApJ](#), **889**, L1
- Licquia T. C., Newman J. A., 2015, [ApJ](#), **806**, 96
- Liu W., et al., 2016, [The Astrophysical Journal](#), **834**, 33
- Lochhaas C., Bryan G. L., Li Y., Li M., Fielding D., 2020, [Monthly Notices of the Royal Astronomical Society](#), **493**, 1461
- Maller A. H., Bullock J. S., 2004, [MNRAS](#), **355**, 694
- Marra R., et al., 2021, [Monthly Notices of the Royal Astronomical Society](#), **508**, 4938
- Mathews W. G., Prochaska J. X., 2017, [ApJ](#), **846**, L24
- Mathur S., Das S., Gupta A., Krongold Y., 2023, [Monthly Notices of the Royal Astronomical Society: Letters](#), **525**, L11
- Miller M. J., Bregman J. N., 2013, [ApJ](#), **770**, 118
- Miller M. J., Bregman J. N., 2015, [The Astrophysical Journal](#), **800**, 14
- Mohapatra R., Sharma P., 2019, [MNRAS](#), **484**, 4881
- Mohapatra R., Federrath C., Sharma P., 2021, [MNRAS](#), **500**, 5072
- Mohapatra R., Jetty M., Sharma P., Federrath C., 2022, [MNRAS](#), **510**, 3778
- Mohapatra R., Sharma P., Federrath C., Quataert E., 2023, [arXiv e-prints](#), p. [arXiv:2302.09380](#)
- Muzahid S., Fonseca G., Roberts A., Rosenwasser B., Richter P., Narayanan A., Churchill C., Charlton J., 2018, [Monthly Notices of the Royal Astronomical Society](#), **476**, 4965
- Nakashima S., Inoue Y., Yamasaki N., Sofue Y., Kataoka J., Sakai K., 2018, [ApJ](#), **862**, 34
- Nateghi H., Kacprzak G. G., Nielsen N. M., Muzahid S., Churchill C. W., Pointon S. K., Charlton J. C., 2020, [Monthly Notices of the Royal Astronomical Society](#), **500**, 3987
- Nelson D., et al., 2020, [MNRAS](#), **498**, 2391
- Nelson D., et al., 2023, [Monthly Notices of the Royal Astronomical Society](#), **522**, 3665
- Nielsen N. M., Churchill C. W., Kacprzak G. G., Murphy M. T., Evans J. L., 2016, [ApJ](#), **818**, 171
- Nielsen N. M., Kacprzak G. G., Muzahid S., Churchill C. W., Murphy M. T., Charlton J. C., 2017, [ApJ](#), **834**, 148
- Ocker S. K., Cordes J. M., Chatterjee S., 2021, [ApJ](#), **911**, 102
- Oppenheimer B. D., Schaye J., Crain R. A., Werk J. K., Richings A. J., 2018, [Monthly Notices of the Royal Astronomical Society](#), **481**, 835
- Ponti G., et al., 2023a, [A&A](#), **670**, A99
- Ponti G., et al., 2023b, [A&A](#), **674**, A195
- Predehl P., et al., 2020, [Nature](#), **588**, 227
- Predehl P., et al., 2021, [A&A](#), **647**, A1
- Péroux C., et al., 2019, [Monthly Notices of the Royal Astronomical Society](#), **485**, 1595
- Qu Z., et al., 2023, [arXiv e-prints](#), p. [arXiv:2306.11274](#)
- Qu Z., et al., 2024, [arXiv e-prints](#), p. [arXiv:2402.08016](#)
- Ramesh R., Nelson D., Pillepich A., 2023, [MNRAS](#), **518**, 5754
- Ravi V., et al., 2023, [arXiv e-prints](#), p. [arXiv:2301.01000](#)
- Rohr E., Pillepich A., Nelson D., Zinger E., Joshi G. D., Ayromlou M., 2023, [Monthly Notices of the Royal Astronomical Society](#), **524**, 3502
- Rubin K. H. R., Weiner B. J., Koo D. C., Martin C. L., Prochaska J. X., Coil A. L., Newman J. A., 2010, [The Astrophysical Journal](#), **719**, 1503
- Rudie G. C., Steidel C. C., Pettini M., Trainor R. F., Strom A. L., Hummels C. B., Reddy N. A., Shapley A. E., 2019, [ApJ](#), **885**, 61
- Saeedzadeh V., et al., 2023, [Monthly Notices of the Royal Astronomical Society](#), **525**, 5677
- Salem M., Bryan G. L., Corlies L., 2015, [Monthly Notices of the Royal Astronomical Society](#), **456**, 582
- Sameer et al., 2021, [MNRAS](#), **501**, 2112
- Sameer et al., 2024, [arXiv e-prints](#), p. [arXiv:2403.05617](#)
- Sarkar K. C., Nath B. B., Sharma P., 2015, [MNRAS](#), **453**, 3827
- Savage B. D., Sembach K. R., 1991, [ApJ](#), **379**, 245
- Schaye J., et al., 2015, [MNRAS](#), **446**, 521
- Sharma P., McCourt M., Quataert E., Parrish I. J., 2012a, [MNRAS](#), **420**, 3174
- Sharma P., McCourt M., Parrish I. J., Quataert E., 2012b, [MNRAS](#), **427**, 1219
- Singh P., Majumdar S., Nath B. B., Silk J., 2018, [MNRAS](#), **478**, 2909
- Smith R. K., Brickhouse N. S., Liedahl D. A., Raymond J. C., 2001, [ApJ](#), **556**, L91
- Sormani M. C., Sobacchi E., Pezzulli G., Binney J., Klessen R. S., 2018, [MNRAS](#), **481**, 3370
- Stern J., Fielding D., Faucher-Giguère C.-A., Quataert E., 2019, [Monthly Notices of the Royal Astronomical Society](#), **488**, 2549
- Stoeck J. T., Keeney B. A., Danforth C. W., Shull J. M., Froning C. S., Green J. C., Penton S. V., Savage B. D., 2013, [ApJ](#), **763**, 148
- Strawn C., Roca-Fàbrega S., Primack J., 2022, [Monthly Notices of the Royal Astronomical Society](#), **519**, 1
- Tchernyshyov K., et al., 2022, [The Astrophysical Journal](#), **927**, 147
- Tumlinson J., et al., 2011a, [Science](#), **334**, 948
- Tumlinson J., et al., 2011b, [ApJ](#), **733**, 111
- Tumlinson J., et al., 2013, [The Astrophysical Journal](#), **777**, 59
- Tumlinson J., Peebles M. S., Werk J. K., 2017, [Annual Review of Astronomy and Astrophysics](#), **55**, 389
- Tuttle S., et al., 2019, [Astro2020: Decadal Survey on Astronomy and Astrophysics](#), **54**, 041
- Vijayan A., Li M., 2022, [MNRAS](#), **510**, 568
- Voit G. M., 2019, [ApJ](#), **880**, 139
- Wakker B. P., Savage B. D., 2009, [The Astrophysical Journal Supplement Series](#), **182**, 378
- Wakker B. P., Savage B. D., Richter P., Meade M., Sembach K. R., 2003, in Rosenberg J. L., Putman M. E., eds, *Astrophysics and Space Science Library Vol. 281, The IGM/Galaxy Connection. The Distribution of Baryons at z=0*. p. 183 ([arXiv:astro-ph/0208009](#)), doi:10.1007/978-94-010-0115-1_33
- Weiner B. J., et al., 2009, [The Astrophysical Journal](#), **692**, 187
- Werk J. K., Prochaska J. X., Thom C., Tumlinson J., Tripp T. M., O'Meara J. M., Meiring J. D., 2012, [ApJS](#), **198**, 3
- Werk J. K., Prochaska J. X., Thom C., Tumlinson J., Tripp T. M., O'Meara J. M., Peebles M. S., 2013, [ApJS](#), **204**, 17
- Werk J. K., et al., 2014, [ApJ](#), **792**, 8
- Werk J. K., et al., 2016, [ApJ](#), **833**, 54
- Wu X., McQuinn M., 2022, [arXiv e-prints](#), p. [arXiv:2209.04455](#)
- Yamasaki S., Totani T., 2020, [ApJ](#), **888**, 105
- Yang Y., Ji S., 2023, [MNRAS](#), **520**, 2148
- Yao J. M., Manchester R. N., Wang N., 2017, [ApJ](#), **835**, 29
- Zabl J., et al., 2019, [MNRAS](#), **485**, 1961
- Zahedy F. S., Chen H.-W., Johnson S. D., Pierce R. M., Rauch M., Huang Y.-H., Weiner B. J., Gauthier J.-R., 2019, [MNRAS](#), **484**, 2257
- ZuHone J. A., Miller E. D., Bulbul E., Zhuravleva I., 2018, [ApJ](#), **853**, 180
- van de Voort F., Springel V., Mandelker N., van den Bosch F. C., Pakmor R., 2018, [Monthly Notices of the Royal Astronomical Society: Letters](#), **482**, L85

APPENDIX A: ASTROPLASMA CODE REPOSITORY

AstroPlasma is a publicly hosted astrophysical plasma modeling code that aims to model the physical conditions and absorption and emission properties of the CGM plasma. *AstroPlasma* uses a database of pre-computed CLOUDY models (Ferland et al. 2017) to interpolate plasma properties in typical CGM conditions. This provides a fast, computationally inexpensive interface to perform on-the-fly calculations of plasma properties needed to generate observables from different CGM models/simulation data. *AstroPlasma* is written in a flexible and user-friendly manner in Python, and its database and range of applicability can be updated and enhanced as per the need. Here, we illustrate some of the basic usage of *AstroPlasma*. Interested readers can find more about it at the *AstroPlasma* *GitHub* repository. We aim to maintain and expand *AstroPlasma*, making it a useful tool for the community. We welcome contributions in the form of pull requests and issues.

A1 Ionization modeling

AstroPlasma can be used to calculate the ionization state of ions

for given conditions. As an example, in the following Python code snippet, we calculate the ionization fraction of OVI.

```
1 # Import AstroPlasma Ionization module
2 from astro_plasma import Ionization
3
4 fIon = Ionization.interpolate_ion_frac
5
6 nH = 1.2e-04 # Hydrogen number density in cm^-3
7 temperature = 4.2e+05 # Temperature in kelvin
8 metallicity = 0.99 # Metallicity wrt solar
9 redshift = 0.001 # Cosmological redshift
10 mode = "CIE" # Ionization equilibrium: CIE/PIE
11
12 fOVI = fIon(nH = nH,
13            temperature = temperature,
14            metallicity = metallicity,
15            redshift = redshift,
16            element = "OVI",
17            ) # This value is in log10
18 print(f"f_OVI = {pow(10, fOVI):.3e}")
```

It is also possible to directly calculate the number density of a specific ion (up to Zn with atomic number 30), all ions, electrons, or all neutral species using AstroPlasma. Equilibrium ionization is also taken into account while calculating the mean mass of different species in the plasma. The following code snippet illustrates the usage of AstroPlasma to calculate these quantities. None of these calculations involve any real-time plasma calculations but are interpolated from the CLOUDY database.

```
1 from astro_plasma import Ionization
2
3 num_dens = Ionization.interpolate_num_dens
4
5 ne = num_dens(nH = nH,
6              temperature = temperature,
7              metallicity = metallicity,
8              redshift = redshift,
9              mode = mode,
10             part_type = "electron",
11             )
12 n = num_dens(nH = nH,
13             temperature = temperature,
14             metallicity = metallicity,
15             redshift = redshift,
16             mode = mode,
17             part_type = "all",
18             )
19 ni = num_dens(nH = nH,
20              temperature = temperature,
21              metallicity = metallicity,
22              redshift = redshift,
23              mode = mode,
24              part_type = "ion",
25              )
26
27 print(f"Free electron density = {ne:.3e} cm^-3")
28 print(f"Total particle density = {n:.3e} cm^-3")
29 print(f"Total ion density = {ni:.3e} cm^-3")
30
31 mean_mass = Ionization.interpolate_mu
32
33 mu = mean_mass(nH = nH,
34               temperature = temperature,
35               metallicity = metallicity,
```

```
36 redshift = redshift,
37 mode = mode,
38 part_type = "all",
39 )
40 print(f"Mean particle mass = {mu:.2f} mp")
```

Presently, AstroPlasma only supports purely collisional and photo+collisional ionization equilibrium (CIE/PIE) conditions, using the HM12 photo-ionizing extragalactic background radiation from [Haardt & Madau \(2012\)](#). In the future, we plan to incorporate effects of different photo-ionizing background radiation (like [Khaire & Srianand 2019](#); [Faucher-Giguère 2020](#)), and also non-equilibrium ionization in AstroPlasma.

A2 Spectral energy distribution (SED) generation

AstroPlasma can also calculate the spectral energy distribution (SED) of the emitted radiation from a one-zone plasma. In order to generate the SED of the whole CGM, we add up emissions from multiple such one-zones weighed by their volume. The plasma is assumed to be optically thin, and we do not account for radiative transfer. Since no real-time plasma calculation is involved in spectrum generation, using AstroPlasma is relatively fast compared to on-the-fly calculation of chemical networks.

```
1 from astro_plasma import EmissionSpectrum
2
3 gen_spectrum =
4     ↪ EmissionSpectrum.interpolate_spectrum
5
6 spectrum = gen_spectrum(nH = nH,
7                        temperature = temperature,
8                        metallicity = metallicity,
9                        redshift = redshift,
10                       mode = mode
11                       ) # Generate spectrum
12
13 import matplotlib.pyplot as plt
14
15 plt.loglog(spectrum[:,0], spectrum[:,1])
16 plt.xlabel(r"Energy (keV)")
17 plt.ylabel(r"Emissivity $4 \pi \nu_j \nu_{\nu} (\text{erg})$")
18 plt.xlim(xmin = 1.0e-10, xmax=3.2)
19 plt.show()
```

APPENDIX B: POWER-LAW DENSITY PROFILES AND COLUMN DENSITIES

The three-phase, one-zone model of the CGM introduced in section 3 assumes a constant density for all the CGM gas. However, this assumption can be relaxed easily if we assume the plasma distribution as a function of radius has a gradual variation. Here, we outline the method to include a radially symmetric power-law density profile for the CGM gas.

We keep the CGM mass fixed and spread it with a power-law density profile. This allows us to write the radial number density of the CGM gas $n(r)$ as

$$n(r) = n_0 \left(1 - \frac{\alpha}{3}\right) \frac{1 - \left(\frac{r_0}{r_{\text{CGM}}}\right)^3}{1 - \left(\frac{r_0}{r_{\text{CGM}}}\right)^{3-\alpha}} \left(\frac{r}{r_{\text{CGM}}}\right)^{-\alpha}, \quad (\text{B1})$$

where n_0 is the constant number density of the CGM gas in the one-zone model, r_0 and r_{CGM} are the inner and outer radii of the CGM respectively, and α is the power-law index, i.e., $n(r) \propto r^{-\alpha}$. We stick to the [FSM17](#) prescription for r_{CGM} , i.e., $r_{\text{CGM}} = 1.1 r_{200}$.

Assuming that the ion densities also follow power-law profiles (possibly different power-law indices for different phases), it is straightforward to calculate the column density $N(b)$ of any ion using the following integral at any given impact parameter b ,

$$N(b) = 2 \int_b^{r_{\text{CGM}}} dr \frac{rn(r)}{\sqrt{r^2 - b^2}}. \quad (\text{B2})$$

Substituting Eq. B1 into Eq. B2, we get the following expression containing transcendental functions,

$$N(b) = n_0 r_{\text{CGM}} \left(1 - \frac{\alpha}{3}\right) \frac{1 - \left(\frac{r_0}{r_{\text{CGM}}}\right)^3}{1 - \left(\frac{r_0}{r_{\text{CGM}}}\right)^{3-\alpha}} \Gamma\left(\frac{\alpha-1}{2}\right) \times \left[\frac{\sqrt{\pi}}{\left(\frac{b}{r_{\text{CGM}}}\right)^{\alpha-1} \Gamma\left(\frac{\alpha}{2}\right)} - {}_2\tilde{F}_1\left(\frac{1}{2}, \frac{\alpha-1}{2}; \frac{\alpha+1}{2}; \left(\frac{b}{r_{\text{CGM}}}\right)^2\right) \right], \quad (\text{B3})$$

where Γ denotes gamma function and ${}_2\tilde{F}_1$ is the *Regularized hypergeometric function*.¹²

The density profile introduced in Eq. B1 can also be thought of as a model for the Milky Way CGM. Just like Eq. B2, which applies for an external galaxy, we make equivalent estimates for Milky Way observables from the solar system location. These observables include the emission and dispersion measures generated from our model, which can then be directly compared with Milky Way observations along any line of sight.

We denote s as the distance between an observer at the position of the solar system and any point along a sightline in Galactic coordinates (l, b) . This same point has spherical coordinates (r, θ, ϕ) with respect to the Galactic center. Converting between spherical and Galactic coordinates, $s \sin b = r \cos \theta$, and using the law of sines for a triangle (see Fig. BA1 & Fig. A1 in [Sarkar et al. 2015](#)), we can write

$$\frac{R_0}{\sin(\phi - l)} = \frac{s \cos b}{\sin \phi} = \frac{r \sin \theta}{\sin l}, \quad (\text{B4})$$

where R_0 is the distance between the sun and the Galactic center (≈ 8 kpc). Eq. B4 combined with

$$r^2 = s^2 + R_0^2 - 2R_0 s \cos b \cos l, \quad (\text{B5})$$

where R_0 is the distance between the sun and the Galactic center (≈ 8 kpc), can let us express s , θ and ϕ in terms of l , b , r and R_0 .

Let the function $f[n(r)]$ (which implicitly depends on its distance from the Galactic center) be any observable from our spherically symmetric model integrated along a line of sight, e.g., $n_e(r)n_H(r)$ for emission measure or $n_e(r)$ for dispersion measure.

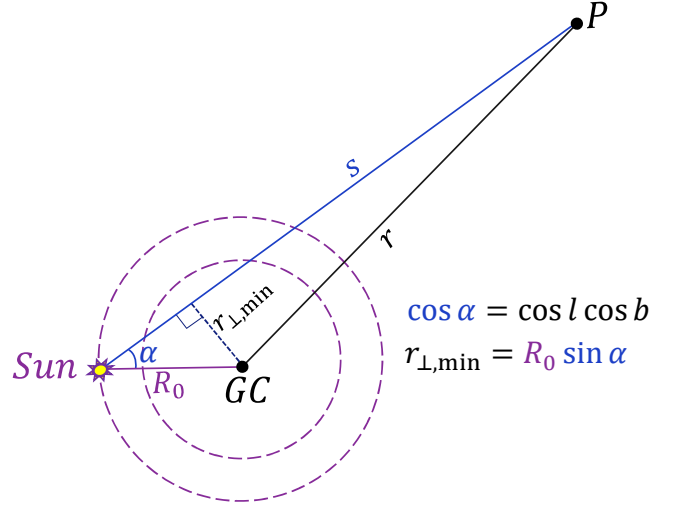


Figure BA1. The relevant geometry to convert the LOS integral (along s , distance along LOS) to an integral involving r (distance from Galactic center). For any Galactic coordinates (l, b) , the angle α satisfies $\cos \alpha = \cos l \cos b$.

Using Eq. B5, we can write the line of sight integral as,¹³

$$I(l, b) = \int_{R_0}^{r_{\text{CGM}}} dr \frac{r f[n(r)]}{\sqrt{r^2 - r_{\perp, \min}^2}} \quad (\text{B6})$$

$$+ \begin{cases} 2 \int_{r_{\perp, \min}}^{R_0} dr \frac{r f[n(r)]}{\sqrt{r^2 - r_{\perp, \min}^2}}; & l \in [0^\circ, 90^\circ) \cup (270^\circ, 360^\circ) \\ 0; & l \in [90^\circ, 270^\circ] \end{cases}$$

where $r_{\perp, \min} = R_0 \sqrt{1 - \cos^2 l \cos^2 b}$ is the minimum perpendicular distance of a sightline along (l, b) from the Galactic center (see Fig. BA1). Note that the sightlines towards the Galactic center (first and fourth quadrants) have an additional contribution from smaller r . Eq. B6 can be numerically integrated to estimate the emission and dispersion measures or surface brightness for different CGM profiles;¹⁴ e.g., a power-law (with index α) profile for our one-zone, three-phase model. A comparison of this model with observations is compiled in Tab. 4.

APPENDIX C: IONIZATION & COOLING FUNCTION

Here we discuss the effects of photo+collisional ionization on different ion fractions, particularly OVI and MgII. We assume the Haardt-Madau extragalactic UV photo-ionizing background ([Haardt & Madau 2012](#)) at a redshift of 0.2. As illustrated in Fig. CA1, in the absence of any photo-ionizing background radiation, the ionization fractions of both OVI and MgII are independent of gas density. The ionization fraction of OVI and MgII are oppositely affected by the photo-ionizing background. OVI is an intermediate ion (tracing warm gas $\sim 10^{5.5}$ K) and its ionization fraction is significantly enhanced at temperatures $\lesssim 10^{5.5}$ K by the photo-ionizing background. On the other hand, since photo-ionizing background

¹² For reference, see [scipy documentation](#) on Hypergeometric function and [Wolfram MathWorld](#) article on Regularized hypergeometric function.

¹³ We use Simpson's rule with r uniformly sampled in log-space to numerically evaluate Eq. B6.

¹⁴ The terms (including the factor 2 in the second term) in Eq. B6 are only correct for a spherically symmetric profile. Otherwise, for any chosen (l, b) sightline, the functional relations $\theta(r)$ and $\phi(r)$ using Eq. B4 need to be explicitly considered.

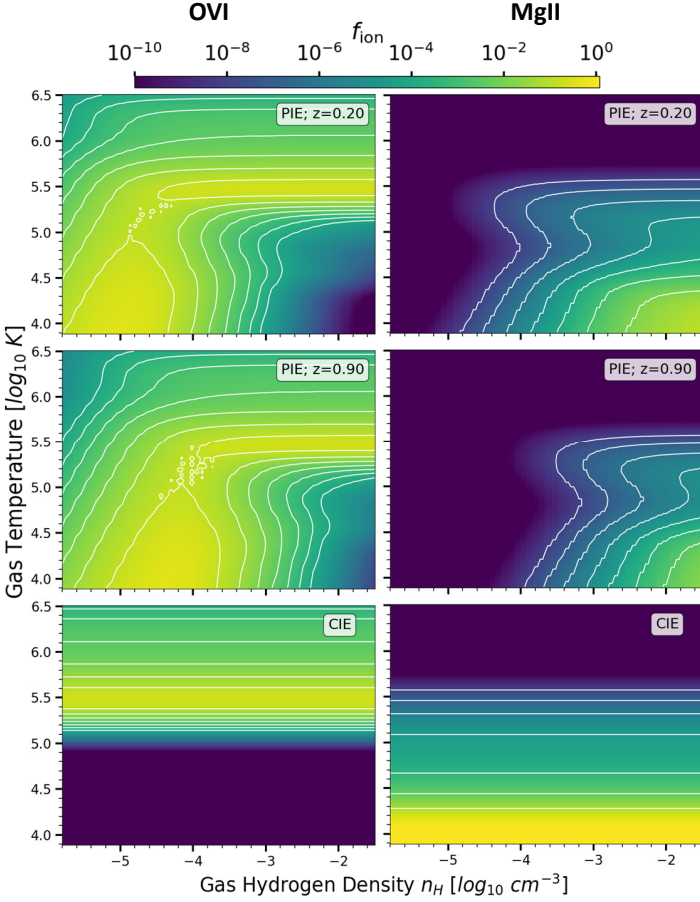


Figure CA1. The ion fraction of OVI (left panels) and MgII (right panels) as a function of hydrogen number density n_H and gas temperature generated using *AstroPlasma*. The bottom row shows equilibrium values with only collisional ionization (CIE) while the top two rows show equilibrium values with photo+collisional ionization (PIE) in Haardt-Madau extragalactic UV background (Haardt & Madau 2012) at $z = 0.2$ and 0.9 . The strength of the UV background increases with redshift.

increases the overall ionization of the plasma, it depletes the amount of low ions like MgII (tracing cold gas $\sim 10^4$ K), especially at low densities $n_H \lesssim 10^{-4} \text{ cm}^{-3}$. Further, the strength of the ionizing background radiation increases with redshift, and its effect is also illustrated in Fig. CA1 (see Strawn et al. 2022 and Fig. 5 from Faerman et al. 2020 for more discussion on this).

Now we show the CLOUDY (Ferland et al. 2017) generated equilibrium cooling function used in this work. For fast computation, we use the CLOUDY generated equilibrium cooling table for plasma at solar metallicity and use an approximate prescription, described in Eq. C1, to scale the cooling value to different metallicities. The robustness of this approximation (C1) is illustrated in the top panel of Fig. CA2. The approximate cooling function at different metallicities (for a fixed density) scaling from solar metallicity is given by

$$\Lambda\left(T, \frac{Z}{Z_\odot}\right) = \left[\mathcal{F}(T) + \{1 - \mathcal{F}(T)\} \left(\frac{Z}{Z_\odot} \right) \right] \Lambda\left(T, \frac{Z}{Z_\odot} = 1\right), \quad (\text{C1})$$

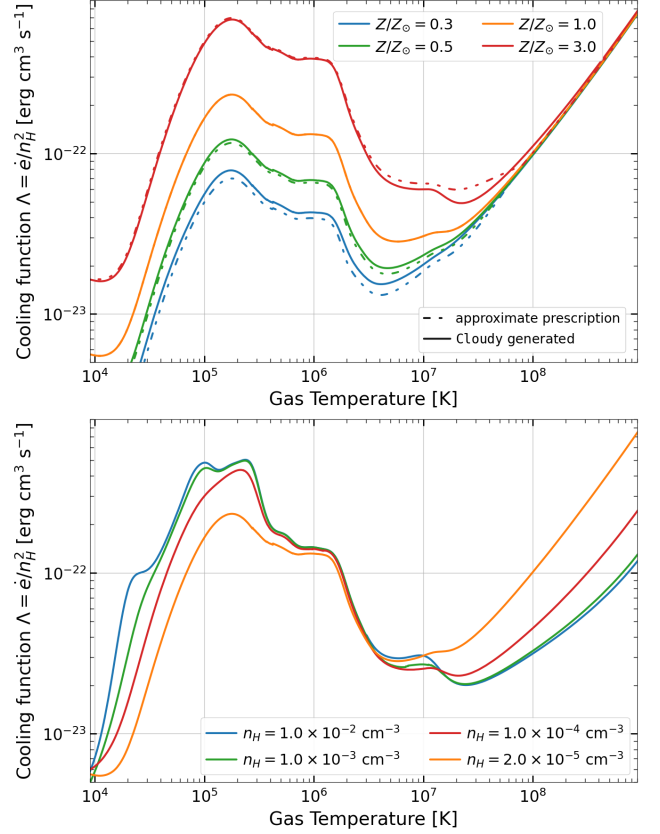


Figure CA2. Equilibrium cooling functions generated using CLOUDY 2017 spectral synthesis code (Ferland et al. 2017). Different cases include collisional+photo-ionization in the presence of Haardt-Madau extragalactic UV background (Haardt & Madau 2012) at $z = 0.2$. *Top panel:* Demonstration of the robustness of our approximate prescription (Eq. C1) that scales the cooling function for different metallicities. The approximate cooling functions (dot-dashed lines) closely follow the actual CLOUDY generated cooling curve (solid lines). *Bottom panel* shows the equilibrium cooling functions at different hydrogen number densities. Due to the presence of the photo-ionizing background, the cooling functions become weakly dependent on the gas density. For both panels and across this work, we use the cooling function fixed to the average density of our fiducial TNG50 halo, $n_H = 2.0 \times 10^{-5} \text{ cm}^{-3}$.

where

$$\mathcal{F}(T) = \begin{cases} 0; & T < 2 \times 10^6 \text{ K} \\ \frac{\log_{10}(T) - \log_{10}(2 \times 10^6)}{\log_{10}(8 \times 10^7) - \log_{10}(2 \times 10^6)}; & 2 \times 10^6 \text{ K} \leq T \leq 8 \times 10^7 \text{ K} \\ 1; & T > 8 \times 10^7 \text{ K} \end{cases}$$

Because of photo-ionization, the cooling function can be significantly affected by a change in the density of the gas, as illustrated in the bottom panel of Fig. CA2. For all the cooling curves used in our work, we set $n_H = 2.0 \times 10^{-5} \text{ cm}^{-3}$, roughly the average density of our TNG50 halo (see Fig. 9).

This paper has been typeset from a \LaTeX file prepared by the author.